The Astrophysical Journal, 730:119 (18pp), 2011 April 1 doi:10.1088/0004-637X/730/2/119

A 3% SOLUTION: DETERMINATION OF THE HUBBLE CONSTANT WITH THE *HUBBLE SPACE TELESCOPE* AND WIDE FIELD CAMERA 3*

Adam G. Riess[1,2], Lucas Macri[3], Stefano Casertano[2], Hubert Lampeitl[4], Henry C. Ferguson[2], Alexei V. Filippenko[5], Saurabh W. Jha[6], Weidong Li[5], and Ryan Chornock[7]

[1] Department of Physics and Astronomy, Johns Hopkins University, Baltimore, MD 21218, USA; ariess@stsci.edu
[2] Space Telescope Science Institute, 3700 San Martin Drive, Baltimore, MD 21218, USA
[3] George P. and Cynthia Woods Mitchell Institute for Fundamental Physics and Astronomy, Department of Physics & Astronomy, Texas A&M University, 4242 TAMU, College Station, TX 77843-4242, USA
[4] Institute of Cosmology and Gravitation, University of Portsmouth, Portsmouth PO1 3FX, UK
[5] Department of Astronomy, University of California, Berkeley, CA 94720-3411, USA
[6] Department of Physics and Astronomy, Rutgers University, 136 Frelinghuysen Road, Piscataway, NJ 08854, USA
[7] Harvard/Smithsonian Center for Astrophysics, 60 Garden Street, Cambridge, MA 02138, USA

Received 2011 January 7; accepted 2011 February 1; published 2011 March 10

ABSTRACT

We use the Wide Field Camera 3 (WFC3) on the *Hubble Space Telescope* (*HST*) to determine the Hubble constant from optical and infrared observations of over 600 Cepheid variables in the host galaxies of eight recent Type Ia supernovae (SNe Ia), providing the calibration for a magnitude–redshift relation based on 253 SNe Ia. Increased precision over past measurements of the Hubble constant comes from five improvements: (1) more than doubling the number of infrared observations of Cepheids in the nearby SN hosts; (2) increasing the sample size of ideal SN Ia calibrators from six to eight; (3) increasing by 20% the number of Cepheids with infrared observations in the megamaser host NGC 4258; (4) reducing the difference in the mean metallicity of the Cepheid comparison samples between NGC 4258 and the SN hosts from $\Delta\log[\mathrm{O/H}] = 0.08$ to 0.05; and (5) calibrating all optical Cepheid colors with a single camera, WFC3, to remove cross-instrument zero-point errors. The result is a reduction in the uncertainty in H_0 due to steps beyond the first rung of the distance ladder from 3.5% to 2.3%. The measurement of H_0 via the geometric distance to NGC 4258 is 74.8 ± 3.1 km s^{-1} Mpc^{-1}, a 4.1% measurement including systematic uncertainties. Better precision independent of the distance to NGC 4258 comes from the use of two alternative Cepheid absolute calibrations: (1) 13 Milky Way Cepheids with trigonometric parallaxes measured with *HST*/fine guidance sensor and *Hipparcos* and (2) 92 Cepheids in the Large Magellanic Cloud for which multiple accurate and precise eclipsing binary distances are available, yielding 74.4 ± 2.5 km s^{-1} Mpc^{-1}, a 3.4% uncertainty including systematics. Our best estimate uses all three calibrations but a larger uncertainty afforded from any two: $H_0 = 73.8 \pm 2.4$ km s^{-1} Mpc^{-1} including systematic errors, corresponding to a 3.3% uncertainty. The improved measurement of H_0, when combined with the *Wilkinson Microwave Anisotropy Probe* (*WMAP*) 7 year data, results in a tighter constraint on the equation-of-state parameter of dark energy of $w = -1.08 \pm 0.10$. It also rules out the best-fitting gigaparsec-scale void models, posited as an alternative to dark energy. The combined H_0 + *WMAP* results yield $N_{\mathrm{eff}} = 4.2 \pm 0.7$ for the number of relativistic particle species in the early universe, a low-significance excess for the value expected from the three known neutrino flavors.

Key words: cosmological parameters – dark energy – distance scale – galaxies: distances and redshifts – stars: variables: Cepheids – supernovae: general

Online-only material: machine-readable table

1. INTRODUCTION

Measurements of the expansion history, $H(z)$, from Type Ia supernovae (SNe Ia) provide crucial, empirical constraints to help guide the emerging cosmological model. While high-redshift SNe Ia reveal that the universe is now accelerating (Riess et al. 1998; Perlmutter et al. 1999), nearby ones provide the most precise measurements of the present expansion rate, H_0.

Recently, high-redshift measurements from the cosmic microwave background radiation (CMB), baryon acoustic oscillations (BAOs), and SNe Ia have been used to derive a cosmological model-dependent *prediction* of the value of H_0 (e.g., Komatsu et al. 2011). They are not, however, a substitute for its *measurement* in the local universe. Such forecasts of H_0 from the high-redshift universe also make specific assumptions about unsettled questions: the nature of dark energy, the global geometry of space, and the basic properties of neutrinos (number and mass). Instead, we can gain insights into these unknowns from a precise, local measurement of H_0. The most precise measurements of H_0 have come from distance ladders which calibrate the luminosities of nearby SNe Ia through *Hubble Space Telescope* (*HST*) observations of Cepheids in their host galaxies (see Freedman & Madore 2010 for a review).

In the early Cycles of *HST*, the SN Ia *HST* Calibration Program (Sandage et al. 2006, hereafter SST) and the *HST* Key Project (Freedman et al. 2001, hereafter KP) each calibrated H_0 via Cepheids and SNe Ia using the Wide Field Planetary Camera 2 (WFPC2) and the Large Magellanic Cloud (LMC) as the first rung on their distance ladder. Unfortunately, the LMC was not an ideal anchor for the cosmic ladder because its distance was constrained to only 5% to 10% (Gibson 2000); its Cepheids (observed from the ground) are of shorter mean

* Based on observations with the NASA/ESA *Hubble Space Telescope*, obtained at the Space Telescope Science Institute, which is operated by AURA, Inc., under NASA contract NAS 5-26555.

period ($\Delta\langle P\rangle \approx 25$ days), and lower metallicity ($\Delta[\mathrm{O/H}] = 0.4$) than those of the spiral galaxies hosting nearby SNe Ia. These differences and uncertainties between ground-based and space-based photometric zero points introduced a 7% systematic error in the determinations of H_0 obtained by those teams (see Section 4). Additional uncertainty arose from the unreliability of the measurements from several of the SNe Ia selected by SST, which were *photographically* observed, highly reddened, atypical, or discovered after peak brightness. Only three SNe Ia (SNe 1990N, 1981B, and 1998aq) from the SST sample lacked these shortcomings, defining only a small set of nearby SNe suitable to calibrate H_0. Despite careful work, the teams' estimates of H_0, each with an uncertainty of $\sim$10%, differed from each other's by 20%, due to the aforementioned systematic errors. Additional progress required rebuilding the distance ladder to address these systematic errors.

The installation of the Advanced Camera for Surveys (ACS) extended the range of *HST* for observing Cepheids, reduced their crowding with finer pixel sampling, and increased their rate of discovery by doubling the field of view. In Cycle 11, members of our team began using ACS to measure Cepheids at optical wavelengths in the hosts of more modern SNe Ia (SN 1994ae by Riess et al. 2005; SN 1995al and SN 2002fk by Riess et al. 2009b) and in a more ideal anchor galaxy (NGC 4258 by Macri et al. 2006).

In *HST* Cycle 15, we began the "Supernovae and H_0 for the Equation of State" (SH0ES) project to measure H_0 to better than 5% precision by addressing the largest remaining sources of systematic error. The SH0ES program constructed a refurbished distance ladder from high-quality light curves of SNe Ia, a geometric distance to NGC 4258 determined through radio (very long baseline interferometry, VLBI) observations of megamasers, and Cepheid variables observed with *HST* in NGC 4258 and in the hosts of recent SNe Ia. The reduction in systematic errors came from additional observations of NGC 4258 and from our use of purely *differential* measurements of the fluxes of Cepheids with similar metallicities and periods throughout all galaxies in our sample. The latter rendered our distance scale insensitive to possible changes in Cepheid luminosities as a function of metallicity or to putative changes in the slope of the period–luminosity relations from galaxy to galaxy. We measured H_0 to 4.7% precision (Riess et al. 2009a, hereafter R09), a factor of two better than previous measurements with *HST* and WFPC2. An alternative analysis using the Benedict et al. (2007) parallax measurements of Milky Way (MW) Cepheids in lieu of the megamaser distance to NGC 4258 showed good agreement, with comparable 5.5% precision.

This result formed a triumvirate of constraints in the *Wilkinson Microwave Anisotropy Probe* (*WMAP*) 7 year analysis (i.e., BAO + H_0 + *WMAP*-7yr) which were selected as the combination most insensitive to systematic errors with which to constrain the cosmological parameters (Komatsu et al. 2011). Together with the *WMAP* constraint on $\Omega_M h^2$, this measurement of H_0 provides a constraint on the nature of dark energy, $w = -1.12 \pm 0.12$ (R09; Komatsu et al. 2011), which is comparable to but independent of the use of high-redshift SNe Ia. It also improves constraints on the properties of the elusive neutrinos, such as the sum of their masses and the number of species (Komatsu et al. 2011).

In *HST* Cycle 17, we used the newly installed Wide Field Camera 3 (WFC3) to increase the sample sizes of both the Cepheids and the SN Ia calibrators along the ladder used by SH0ES to determine H_0. The near-infrared (IR) channel of WFC3 provides an order-of-magnitude improvement in efficiency for follow-up observations of Cepheids over the Near-Infrared Camera and Multi-Object Spectrograph (NICMOS), while the finer pixel scale of the visible channel (relative to ACS) is valuable for reducing the effects of crowding when searching for Cepheids. We present these new observations in Section 2, the redetermination of H_0 in Section 3, and an analysis of the error budget including systematics in Section 4. In Section 5, we address the use of this new measurement along with external data sets to constrain properties of dark energy and neutrinos.

2. WFC3 OBSERVATIONS OF CEPHEIDS IN THE SH0ES PROGRAM

The SH0ES program was developed to improve upon the calibration of the luminosity of SNe Ia in order to better measure the Hubble constant. To ensure a reliable calibration sample, we selected SNe Ia having the following qualities: (1) modern photometric data (i.e., photoelectric or CCD), (2) observed before maximum brightness, (3) low reddening (implying $A_V < 0.5$ mag), (4) spectroscopically normal, and (5) optical *HST*-based observations of Cepheids in its host galaxy. In addition to providing robust distance measures, these qualities are crucial for producing a calibration sample which is a good facsimile of the SN Ia sample they are used to calibrate—i.e., those defining the modern SN Ia magnitude–redshift relation at $0.01 < z < 0.1$ (e.g., Hicken et al. 2009b).

In *HST* Cycles 16 and 17, we used WFC3, ACS, and WFPC2 to discover Cepheids in two new SN Ia hosts: NGC 5584 (host of SN 2007af; L. M. Macri et al. 2011b, in preparation) and NGC 4038/9 ("the Antennae," host of SN 2007sr; L. M. Macri et al. 2011c, in preparation) whose light curves were presented in Hicken et al. (2009b).[8] We also employed the optical channel of WFC3 to reobserve all previous SN Ia hosts in the calibration sample and NGC 4258. This provided for the first time a calibration of all Cepheid optical and infrared photometry using the same zero points. In the case of some hosts, the additional epoch (obtained well after the prior ones) allowed us to discover previously unidentified, longer period ($P > 60$ days) variables. We also used these observations to search for additional Cepheids in the hosts which previously had the smallest numbers of Cepheids: NGC 3021, NGC 3982, NGC 4536, and NGC 4639 (L. M. Macri et al. 2011a, in preparation). The new observations, together with those from Riess et al. (2009b), Saha et al. (1996, 1997, 2001), Gibson et al. (2000), Stetson & Gibson (2001), and Macri et al. (2006), provide the position, period, and phase of 730 Cepheids in eight hosts with reliable SN Ia data as well as NGC 4258. The Cepheids in each host were typically imaged on 14 epochs in $F555W$ and 2–5 epochs with $F814W$ (except for NGC 4258, which has 12 epochs of $F814W$ data). An illustration of the entire data set used to observe the Cepheids is shown in Figure 1. Having previously determined the positions, periods, and optical magnitudes of these Cepheids, it is highly advantageous to observe their near-IR magnitudes with a single photometric system in order to (1) reduce the differential extinction by a factor of five over visual bands, (2) reduce the possible dependence of Cepheid luminosities on chemical composition

[8] We augmented the Hicken et al. light curve of SN 2007sr with three pre-discovery *V*-band observations from the All-Sky Automated Survey (ASAS) extending to pre-maximum; MJD, mag, error triplets are (4441.85,13.44,0.12), (4448.86,12.65,0.05), and (4452.85,12.73,0.08), respectively.

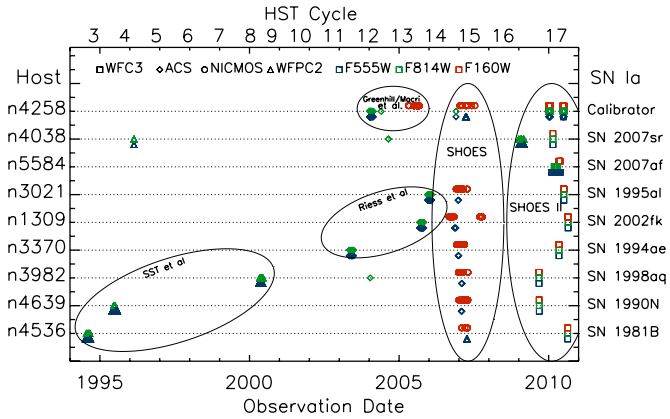

Figure 1. *HST* observations of the host galaxies used to measure H_0. The data employed to observe Cepheids in eight SN Ia hosts and NGC 4258 have been collected over 15 years with four cameras over ∼500 orbits of *HST* time. Two-month long campaigns in $F555W$ and $F814W$ were initially used to discover Cepheids from their light curves. Subsequent follow-up observations in $F555W$ enabled the discovery of Cepheids with $P > 60$ days. Near-IR follow-up data have been used to reduce the effects of host-galaxy extinction and sensitivity to metallicity.

(Marconi et al. 2005), and (3) negate zero-point errors. This was previously done with NICMOS on *HST* in Cycle 15 by R09 for a subset of these Cepheids.

The near-IR channel on WFC3 provides a tremendous gain over NICMOS for the study of extragalactic Cepheids. Photometry of comparable signal-to-noise ratio can be obtained in a quarter of the exposure time. More significant for Cepheid follow-up observations is the factor of 40 increase in the area of WFC3–IR over NICMOS/Camera 2 (NIC2), the channel which offered the best compromise between area and uniform pixel sampling. The one advantage of NIC2 over WFC3–IR is better sampling of the point-spread function (PSF); the 0.″13 pixels of WFC3–IR undersample the *HST* PSF by a factor of 1.6 at 1.6 μm. However, the finer sampling of NIC2 is largely offset by the numerous photometric anomalies unique to that camera, whose subsequent correction leads to correlated noise among neighboring pixels which reduces the independence of the NICMOS pixel sampling. In contrast, the detector of WFC3–IR is much better behaved and pixel sampling noise can be mitigated with dithering.

2.1. WFC3 Data Reduction

Each host galaxy was observed for 2–7 ks with individual exposures 400–700 s in length, using integer and half-pixel dithering between exposures to improve sampling of the PSF (see Table 1). The WFC3 images of the two new hosts, NGC 5584 and NGC 4038, are shown in Figures 2 and 3. Figure 4 shows an example of a host previously observed with NIC2 by R09 and with WFC3–IR in this study.

We developed an automated pipeline to calibrate the raw WFC3 $F160W$ frames. The first step was to pass the data through the STScI-supported *calwf3* pipeline in the *STSDAS* suite of routines in *PyRAF* to remove the bias and dark current, reject cosmic rays through up-the-ramp sampling, and flat-field the data. A small correction to the standard flat-field frame was used to correct the WFC3 "blobs," which are 10% depressions in flux covering ∼1% of the area due to spotting on the surface of the WFC3 Channel Select Mechanism (CSM). Next, we used *multidrizzle* to combine the exposures from each visit into a master image, resampling onto a finer pixel scale while correcting for the known geometric distortions in the camera. We utilized a final pixel scale of 0.″08 pixel^{-1} and an input-to-output fraction of 0.6.

We identified the positions of Cepheids in the WFC3–IR images by deriving geometric transformations from the $F814W$ images to those in $F160W$, successively matching fainter sources to improve the registration. This procedure empirically determined the difference in plate scale between ACS–WFC, WFPC2, WFC3–UVIS, and WFC3–IR. We typically identified more than 100 sources in common, resulting in an uncertainty in the mean position of each Cepheid below 0.03 pixels (<2.4 mas).

We carried out the photometry of Cepheids using the algorithms developed by R09; they employ PSF fitting to model the crowded regions around Cepheids, fixing their positions to those derived from optical data and using artificial-star tests to determine photometric errors and crowding biases. As an example, we show in Figure 5 the *HST* optical image, near-IR image, model, and residuals for eight typical Cepheids spanning a wide range of periods in the SN host NGC 5584. We used the same approach to determine zeropoints as in R09 from the Persson et al. (1998) standard star P330E.

Due to the low amplitudes of their near-IR light curves (<0.3 mag), Cepheid magnitudes determined at random phases provide nearly the same precision as mean fluxes for determining the intercept of their *P–L* relations (Madore & Freedman 1991).[9]

Since we had previously observed with NIC2 many of the Cepheids now observed with WFC3–IR, we can directly compare their $F160W$ photometry on these two systems. Figure 6 shows the magnitude differences for the Cepheids utilized in the *P–L* relations in both R09 and Section 2.2. The mean difference is 0.036 ± 0.027 mag (in the sense that photometry with WFC3 is brighter), with no apparent dependence on Cepheid brightness. While the difference in photometry between instruments may include differences in system zero points, the subsequent determination of H_0 via Cepheids observed with a single instrument in the SN Ia hosts and in NGC 4258 will be independent of instrument zero points. Thus, for the determination of H_0 it is more relevant to calculate the change in magnitudes between Cepheids in NGC 4258 and the SN hosts between WFC3 and NIC2; the measurement of this change is 0.019 ± 0.054 mag.

Table 2 contains relevant parameters for each Cepheid observed with WFC3 $F160W$. The first eight columns give the Cepheid's host, position, identification number (from Macri et al. 2006; Riess et al. 2009b; L. M. Macri et al. 2011a, 2011b, 2011c, in preparation), period, mean $V-I$ color, WFC3 $F160W$ magnitude, and the magnitude uncertainty. Column 9 contains the displacement of the flux centroid in the near-IR data relative to the optical Cepheid position, expressed in units of pixels (1 pixel = 0.″08), a quantity used to refine the determination of the crowding bias. Column 10 gives the photometric crowding bias determined using the artificial-star

[9] In R09, we corrected the measured NICMOS $F160W$ magnitude to the mean-phase magnitude using the Cepheid phase, period, and amplitude from the optical data, the dates of the NICMOS observations, and the Fourier components of Soszyński et al. (2005) which quantify the relations between Cepheid light curves in the optical and near-IR. However, these phase corrections of $\sigma \sim 0.1$ mag were found to be insignificant in the subsequent analysis, since the dispersion of the observed *P–L* relations is $\sigma \sim 0.3$ mag. Here we have not attempted such corrections because the Cepheid phases at the time of the WFC3 $F160W$ observations were too poorly constrained to allow for a significant correction.

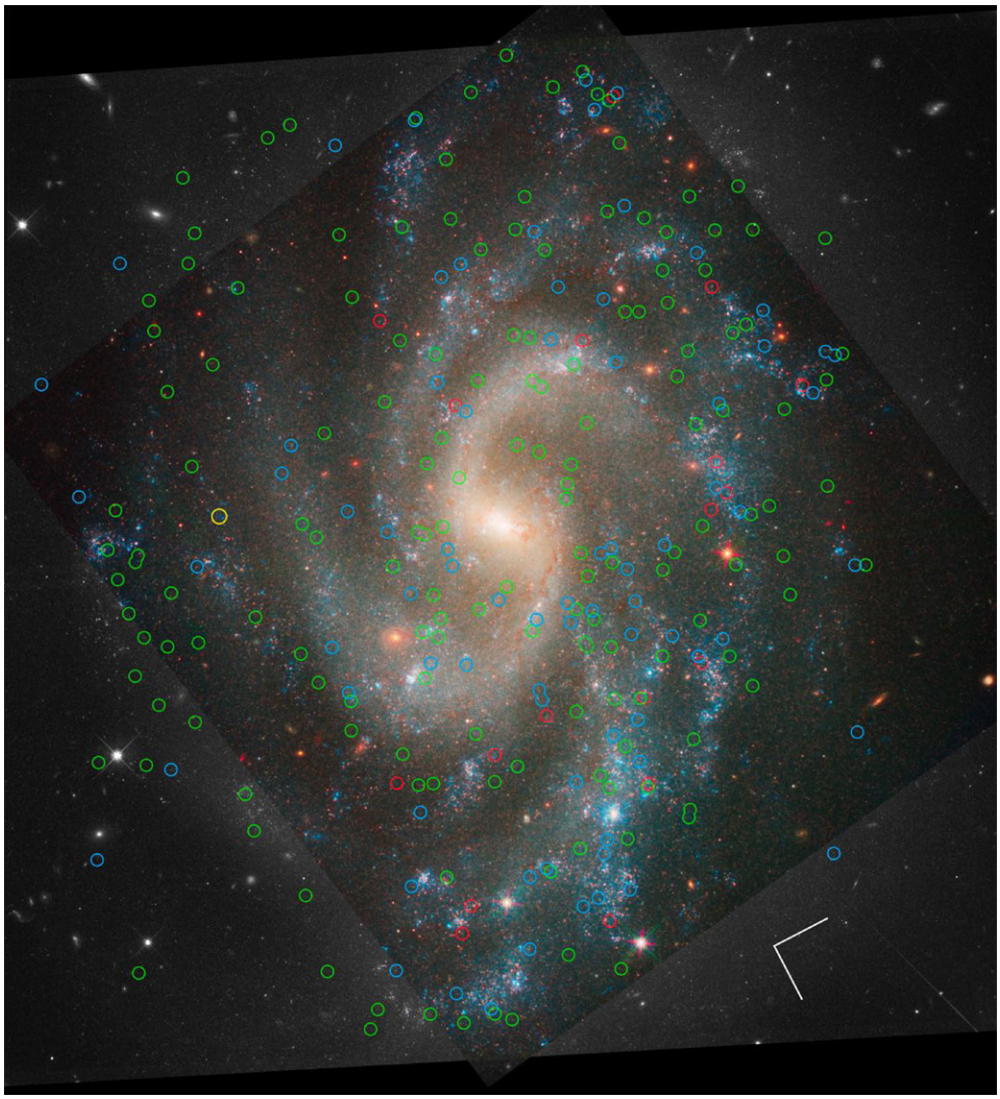

Figure 2. *HST* images of NGC 5584. The positions of Cepheids with periods in the range $P > 60$ days, 30 days $< P < 60$ days, and 10 days $< P < 30$ days are indicated by red, blue, and green circles, respectively. A yellow circle indicates the position of the host galaxy's SN Ia. The orientation is indicated by the compass rose whose vectors have lengths of 15″ and indicate north and east. The black and white regions of the images show the WFC3 optical data and the color includes the WFC3–IR data.

Table 1
Hosts Observed with WFC3–IR $F160W$ by GO-11570

Host	SN Ia	Exp. Time (s)	Optical Data Source
NGC 4536	SN 1981B	2564	Saha et al. (1996)
NGC 4639	SN 1990N	5377	Saha et al. (1997)
NGC 3982	SN 1998aq	4016	Saha et al. (2001)
NGC 3370	SN 1994ae	4374	Riess et al. (2005)
NGC 3021	SN 1995al	4424	Riess et al. (2009b)
NGC 1309	SN 2002fk	6988	Riess et al. (2009b)
NGC 4038/9	SN 2007sr	6794[a]	L. M. Macri et al. (2011c, in preparation)
NGC 5584	SN 2007af	4926	L. M. Macri et al. (2011b, in preparation)
NGC 4258	···	2011[b]	Macri et al. (2006)

Notes.
[a] Data in GO-11577.
[b] Depth per pointing; galaxy covered in 16 pointing mosaic.

tests for each Cepheid's environment (see Section 2.3 of R09) and the displacement tabulated in the previous column; this correction has already been applied to the magnitudes listed in Column 7. Column 11 contains the rms of the residual image, weighted by the inverse distance from the Cepheid position, useful for determining the quality of the crowded-scene fit. Column 12 contains the metallicity parameter, 12 + log [O/H] (Zaritsky et al. 1994), derived from the deprojected

Figure 3. As in Figure 2, for NGC 4038/4039.

galactocentric radii of each Cepheid and the abundance gradient of its host.[10] Column 13 contains a rejection flag used for the *P–L* relations.

2.2. Near-infrared Cepheid Relations

The nine individual *P–L* relations measured with WFC3 $F160W$ and fit with a common slope are shown in Figure 7. Intercepts relative to NGC 4258 are given in Table 3. While 636 Cepheids previously identified at optical wavelengths were measurable[11] in the WFC3–IR $F160W$ images, ∼20% appeared as outliers in the IR *P–L* relations. This is not surprising, as we expect outliers to occur from (1) a complete blend with a bright, red source such as a red giant, (2) a poor model reconstruction of a crowded group when the Cepheid is a small component of the group's flux, (3) objects misidentified as classical Cepheids in the optical (e.g., blended Type II Cepheids), and (4) Cepheids with the wrong period (aliasing or incomplete sampling of a single cycle). As expected, the outlier fraction is greater in WFC3 images than in NIC2 ones because the former contain a larger fraction of Cepheids from crowded regions (such as the nucleus) which yield more outliers and were intentionally avoided in the small, selective NIC2 pointings (see Figure 4).

As in R09, we eliminated outliers >0.75 mag or $>2.5\sigma$ (following Chauvenet's criterion) from an initial fit of the *P–L* relations, refitted the relations and repeated these tests for outliers until convergence. The objects rejected in this way are indicated in the last column of Table 2. This resulted in a reduction of the sample to 484 objects; the next section considers the effect of this rejection on the determination of H_0 and an alternative method for contending with outliers.

3. MEASURING THE HUBBLE CONSTANT

The determination of the Hubble constant follows from the relations given in Section 3 of R09. To summarize, we perform a single, simultaneous fit to all Cepheid and SN Ia data to minimize the χ^2 statistic and measure the parameters of the distance ladder. We express the *j*th Cepheid magnitude in the *i*th

[10] These gradients were published in R09 for NGC 4258 and the previously observed six SN hosts; the values for the new hosts, following the same convention as in Table 12 of that paper, are $12 + \log [O/H] = 8.981 - 0.064(x - 30'')/10''$ for NGC 5584 and $12 + \log [O/H] = 9.129 - 0.043(x - 30'')/10''$ for NGC 4038/9.

[11] Cepheids were considered to be measured if our software reported a possible magnitude for the source with an uncertainty less than 0.7 mag, a model residual with the rms better than 3σ from the distribution of all model residuals, and a crowding correction less than 1.5 mag. While these thresholds are somewhat arbitrary, they are sufficient to remove catastrophic failures in convergence on the measurement of the photometry for a source.

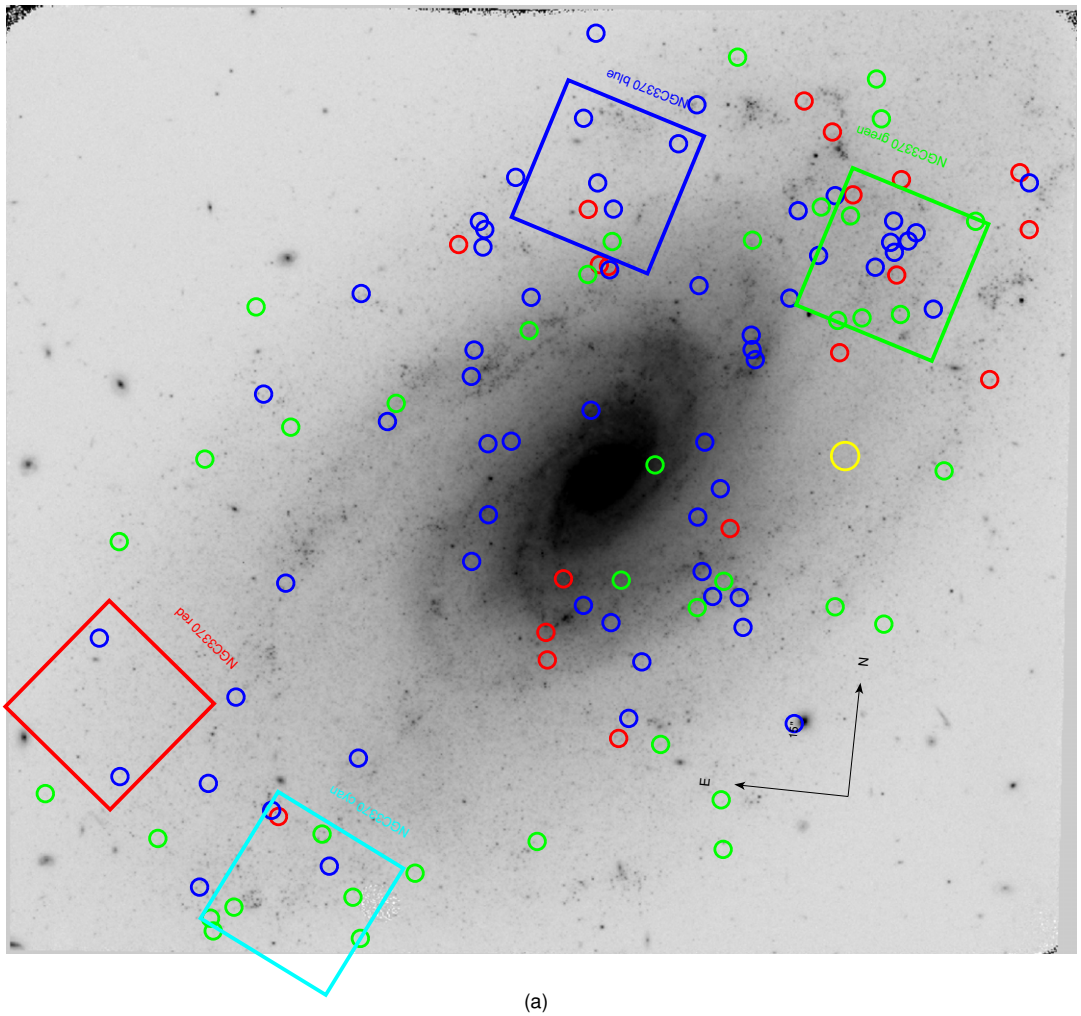

(a)

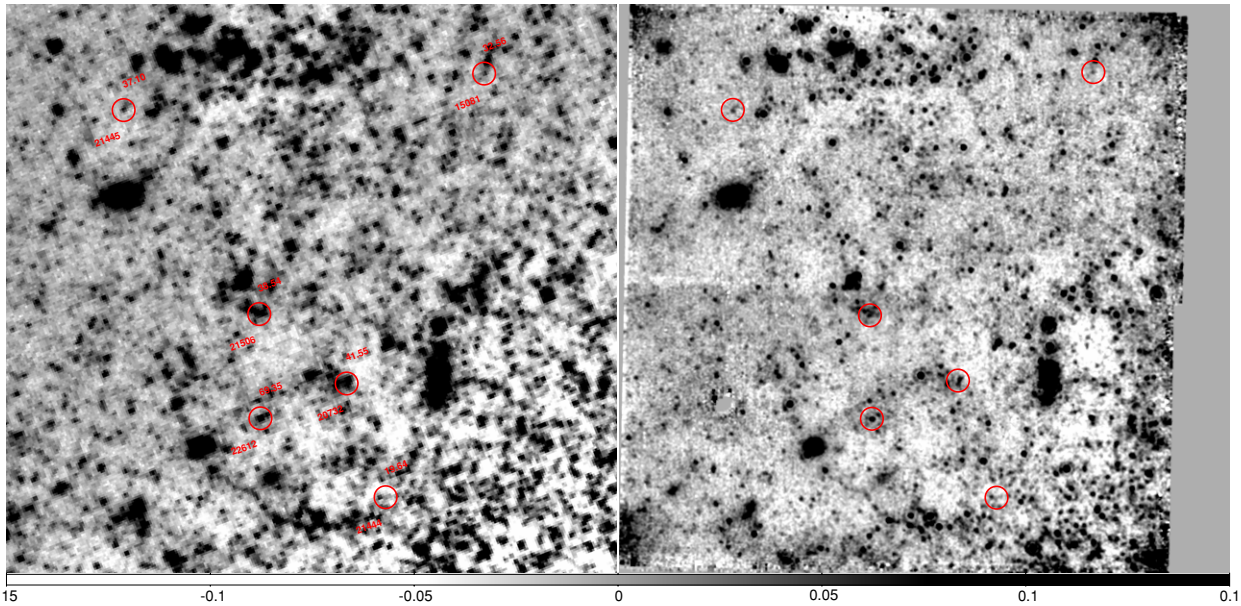

(b)

Figure 4. *HST* WFC3–$F160W$ image of NGC 3370. Upper panel: the positions of Cepheids with periods in the range $P > 60$ days, 30 days $< P < 60$ days, and 10 days $< P < 30$ days are indicated by red, blue, and green circles, respectively. A yellow circle indicates the position of the host galaxy's SN Ia. The orientation is indicated by the compass rose whose vectors have lengths of 15″. The fields of view for the NIC2 follow-up fields from Riess et al. (2009a) are indicated. Lower panel: close-up showing the field of NGC 3370—blue as observed with WFC3–IR (left) and with 4.7 times more exposure time with NIC2 (right).

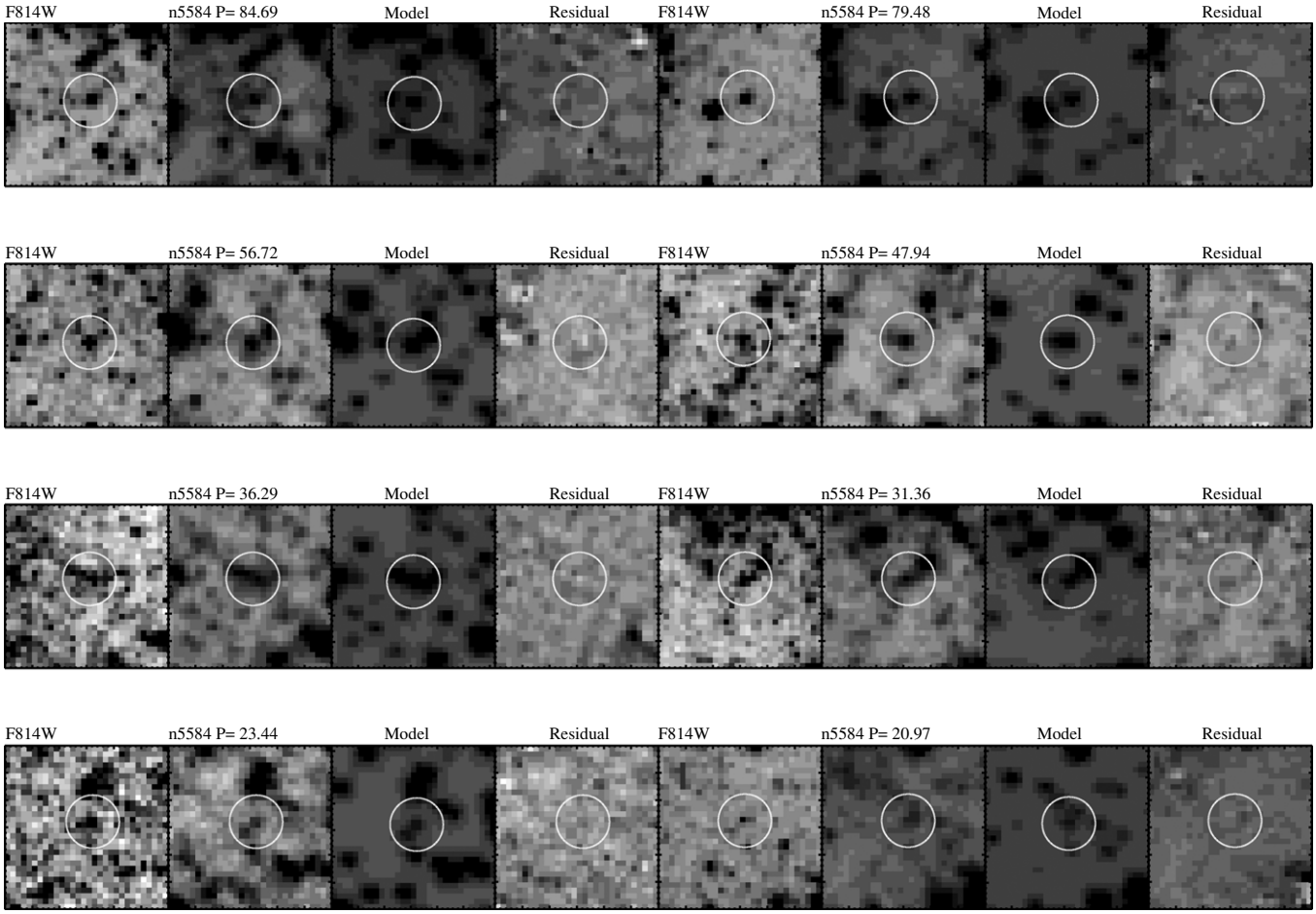

Figure 5. Example of scene modeling for the $\sim 1''$ surrounding typical short, medium, and long-period Cepheids in one WFC3 field, NGC 5584. For each Cepheid, the stamp on the left shows the region around the Cepheid in the optical ($F814W$) and IR ($F160W$), the middle stamp shows the IR model of the stellar sources, and the right stamp is the residual of the IR image minus the model. The position of the Cepheid as determined from the optical data is indicated by the circle.

host as

$$m_{W,i,j} = (\mu_{0,i} - \mu_{0,4258}) + zp_{W,4258} + b_W \log P_{i,j} + Z_W \, \Delta\log[\mathrm{O/H}]_{i,j}, \quad (1)$$

where the "Wesenheit reddening-free" mean magnitude (Madore 1982) is given as

$$m_{W,i,j} = m_{H,i,j} - R(m_{V,i,j} - m_{I,i,j}), \quad (2)$$

and $R \equiv A_H/(A_V - A_I)$. The Cepheid parameters with subscripts i, j are given in Table 2. For a Cardelli et al. (1989) reddening law, a Galactic-like value of $R_V = 3.1$, and the H band corresponding to the WFC3 $F160W$ band, we have $R = 0.410$. In the next section, we consider the sensitivity of H_0 to the value of R_V.

We determine the values of the nuisance parameters b_W and Z_W—which define the relation between Cepheid period, metallicity, and luminosity—by minimizing the χ^2 for the global fit to all Cepheid data. The reddening-free distances, $\mu_{0,i}$, for the hosts relative to NGC 4258 are given by the fit parameters $\mu_{0,i} - \mu_{0,4258}$, while zp_{4258} is the intercept of the P–L relation simultaneously fit to the Cepheids of NGC 4258.

The SN Ia magnitudes in the SH0ES hosts are simultaneously expressed as

$$m^0_{v,i} = (\mu_{0,i} - \mu_{0,4258}) + m^0_{v,4258}, \quad (3)$$

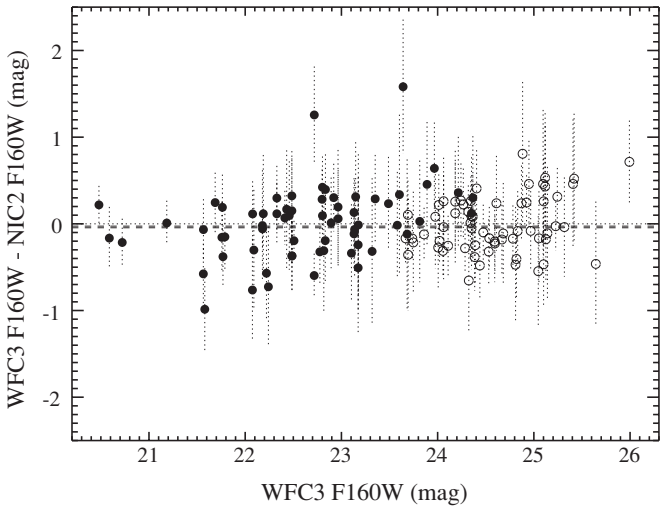

Figure 6. WFC3–IR vs. NIC2 $F160W$ Cepheid photometry. Some of the apparent dispersion results from the random phases of the Cepheids observed with WFC3.

where the value $m^0_{v,i}$ is the maximum-light apparent V-band brightness of an SN Ia in the ith host at the time of B-band peak corrected to the fiducial color and luminosity. This quantity is determined for each SN Ia from its multi-band light curves and

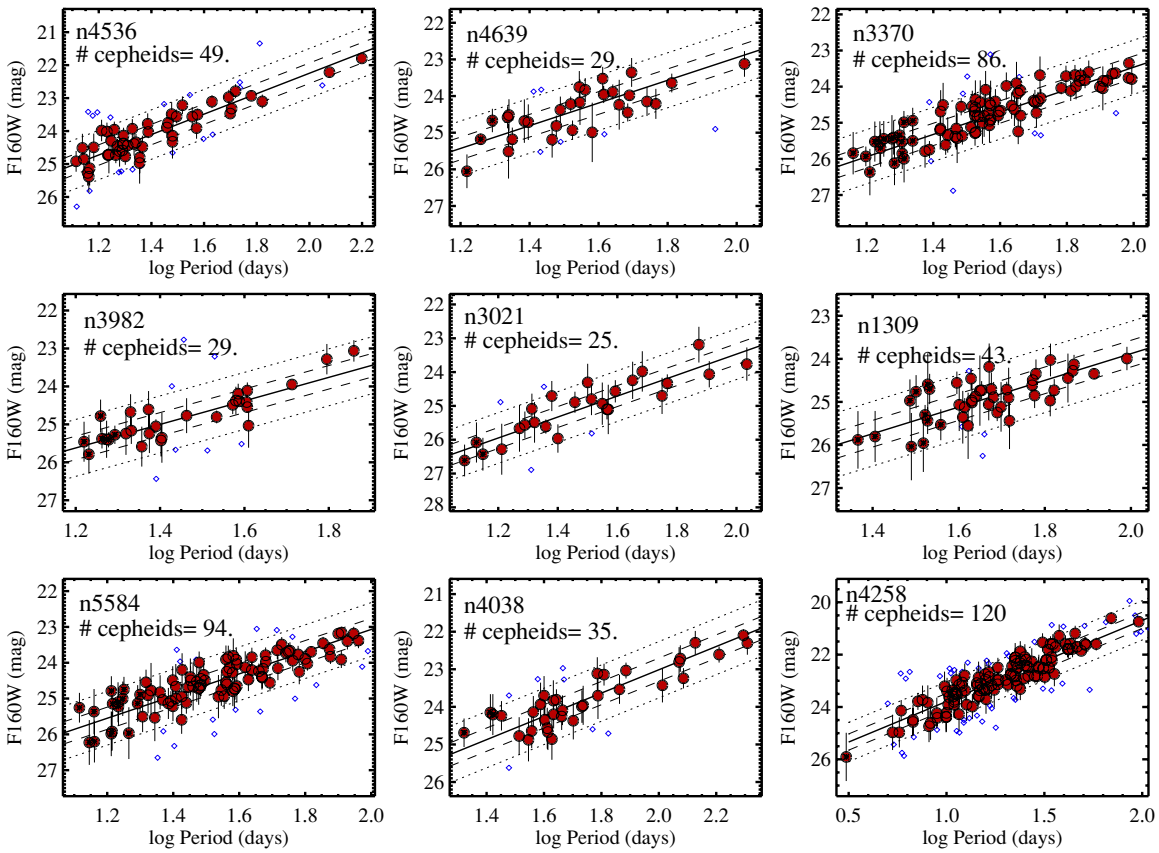

Figure 7. Near-IR Cepheid period–luminosity relations. For the eight SN Ia hosts and the distance-scale anchor, NGC 4258, the Cepheid magnitudes are from the same instrument and filter combination, WFC3 $F160W$. This uniformity allows for a significant reduction in systematic error when utilizing the difference in these relations along the distance ladder. The measured metallicity for all of the Cepheids is comparable to solar ($\log[O/H] \approx 8.9$). A single slope has been fit to the relations and is shown as the solid line. 20% of the objects were outliers from the relations (open diamonds) and are flagged as such for the subsequent analysis. Filled points with asterisks indicate Cepheids whose periods are shorter than the incompleteness limit identified from their optical detection. Dashed lines indicate the average dispersion of 0.3 mag and dotted lines are the 0.75 mag rejection threshold discussed in the text.

Table 2
WFC3–IR Cepheids

Field	α (J2000)	δ (J2000)	ID	P (days)	$V-I$ (mag)	$F160W$ (mag)	σ (mag)	Offset (pixel)	Bias (mag)	IM_{rms}	[O/H]	Flag
n4536	188.590	2.16830	27185	13.00	0.97	24.91	0.31	1.64	0.13	2.16	8.54	
n4536	188.604	2.18312	42353	13.07	0.73	26.29	0.74	3.32	0.37	4.30	8.97	Rej
n4536	188.584	2.18070	50718	13.73	0.88	24.51	0.42	0.88	0.28	11.4	8.64	
n4536	188.583	2.19700	72331	13.91	0.89	24.84	0.44	0.07	0.22	1.40	8.81	
n4536	188.590	2.19545	65694	14.38	0.98	25.26	0.38	2.91	0.39	30.8	8.90	
n4536	188.587	2.18864	58805	14.44	1.13	23.41	0.35	3.94	0.26	47.9	8.78	Rej
n4536	188.586	2.18406	53703	14.53	0.72	25.38	0.47	0.63	0.27	14.9	8.72	
n4536	188.592	2.20025	70938	14.62	0.64	25.81	0.58	2.39	0.30	17.4	8.94	Rej
n4536	188.594	2.17693	40098	14.64	0.95	25.12	0.52	4.40	0.63	12.9	8.72	
n4536	188.597	2.18489	48539	15.03	0.90	23.53	0.31	0.46	0.29	7.28	8.89	Rej

(This table is available in its entirety in a machine-readable form in the online journal. A portion is shown here for guidance regarding its form and content.)

a light curve fitting algorithm, either from the MLCS2k2 (Jha et al. 2007) or from the SALT-II (Guy et al. 2005) prescription (see Section 4.2 for further discussion).

A minor change from R09 is the inclusion of a recently identified, modest relationship between host-galaxy mass and the calibrated SN Ia magnitude. Several studies (Hicken et al. 2009a; Kelly et al. 2010; Lampeitl et al. 2010; Sullivan et al. 2010) have shown the existence of a correlation between the corrected SN magnitude and the mass of its host, with a value of 0.03 mag dex^{-1} in $M_{\rm stellar}$, in the sense that more massive (and metal-rich) hosts produce more luminous SNe. This correlation has been independently detected using both low- and high-redshift samples of SNe Ia, as well as with multiple fitting algorithms. The effect on H_0 is quite small, a decrease of 0.75%, due to the modest difference in mean masses for the nearby hosts (Neill et al. 2009; mean $\log M_{\rm stellar} = 10.0$) and for those that define the magnitude–redshift relation (Sullivan et al. 2010; mean $\log M_{\rm stellar} = 10.5$). We include these corrections based on host-galaxy mass in our present determination of $m^0_{v,i}$, given in Table 3 and Figure 8, normalizing to a fiducial host mass of $\log M_{\rm stellar} = 10.5$ as appropriate for the objects used to measure the Hubble flow.

Table 3
Distance Parameters

Host	SN Ia	Filters	$m^0_{v,i}+5a_v$	σ[a]	$\mu_{0,i}-\mu_{0,4258}$	μ_0 Best
n4536	SN 1981B	*UBVR*	15.147	0.145	1.567 (0.0404)	30.91 (0.07)
n4639	SN 1990N	*UBVRI*	16.040	0.111	2.383 (0.0630)	31.67 (0.08)
n3370	SN 1994ae	*UBVRI*	16.545	0.101	2.835 (0.0284)	32.13 (0.07)
n3982	SN 1998aq	*UBVRI*	15.953	0.091	2.475 (0.0460)	31.70 (0.08)
n3021	SN 1995al	*UBVRI*	16.699	0.113	3.138 (0.0870)	32.27 (0.08)
n1309	SN 2002fk	*BVRI*	16.768	0.103	3.276 (0.0491)	32.59 (0.09)
n5584	SN 2007af	*BVRI*	16.274	0.122	2.461 (0.0401)	31.72 (0.07)
n4038	SN 2007sr	*BVRI*	15.901	0.137	2.396 (0.0567)	31.66 (0.08)
Weighted mean	···	···	···	0.0417	··· (0.0133)	···

Note. [a] For MLCS2k2, 0.08 mag added in quadrature to fitting error.

The simultaneous fit to all Cepheid and SN Ia data via Equations (1) and (3) results in the determination of $m^0_{v,4258}$, which is the expected reddening-free, fiducial, peak magnitude of an SN Ia appearing in NGC 4258. Finally, the Hubble constant is determined from

$$\log H_0 = \frac{\left(m^0_{v,4258} - \mu_{0,4258}\right) + 5a_v + 25}{5}, \quad (4)$$

where $\mu_{4258,0}$ is the independent, geometric distance estimate to NGC 4258 obtained through VLBI observations of water megamasers orbiting its central supermassive black hole (Herrnstein et al. 1999; Humphreys et al. 2005, 2008; Argon et al. 2007; Greenhill 2009). The term a_v is the intercept of the SN Ia magnitude–redshift relation, approximately $\log cz - 0.2m^0_v$ but given for an arbitrary expansion history as

$$a_v = \log cz\left\{1 + \frac{1}{2}\left[1-q_0\right]z - \frac{1}{6}\left[1 - q_0 - 3q_0^2 + j_0\right]z^2 + O(z^3)\right\} - 0.2m^0_v, \quad (5)$$

measured from the set of SN Ia (z, m^0_v) independent of any absolute (i.e., luminosity or distance) scale. As in R09, we determine a_v from a Hubble diagram for 240 SNe Ia from Hicken et al. (2009b) using MLCS2k2 (Jha et al. 2007) or the SALT-II (Guy et al. 2005) prescription to determine m^0_v. Limiting the sample to $0.023 < z < 0.1$ (to avoid the possibility of a local, coherent flow; z is the redshift in the rest frame of the CMB) leaves 140 SNe Ia. (In the next section, we consider a lower cut of $z > 0.01$.) Ganeshalingam et al. (2010) recently published light curves of a large sample of SNe Ia from the Lick Observatory Supernova Search, but there is a large overlap with those given by Hicken et al. (2009b). There are only 13 SNe Ia at $z > 0.023$ not already included in our sample and we have added these to raise the total to 253 SNe Ia. Together with the present acceleration $q_0 = -0.55$ and prior deceleration $j_0 = 1$ (Riess et al. 2007), we find $a_v = 0.697 \pm 0.00201$.

The full statistical error in H_0 is the quadrature sum of the uncertainty in the three *independent* terms in Equation (4): $\mu_{4258,0}$, $m^0_{v,4258}$, and $5a_V$, where $\mu_{4258,0}$ is the geometric distance estimate to NGC 4258 by Herrnstein et al. (1999), claimed by Greenhill (2009) to currently have a 3% uncertainty.

Hui & Greene (2006) point out that the peculiar velocities of SN Ia hosts and their correlations can produce an additional systematic error in the determination of the SN Ia m–z relation used for cosmography. However, by making use of a map of the matter density field, it is possible to correct individual SN Ia redshifts for these peculiar flows (Riess et al. 1997). Neill et al. (2007) made use of the *IRAS* PSCz density field (Branchini et al. 1999) to determine the effect of the density field on the low-redshift SN Ia m–z relation and its impact on the equation-of-state parameter of dark energy, $w = P/(\rho c^2)$ (where P is the pressure and ρc^2 is the energy density). Using their results for a light-to-matter bias parameter $\beta = 0.5$ and the dipole from Pike & Hudson (2005) results in an increase of the mean velocity of the low-redshift sample and in the Hubble constant by 0.4% over the case of uncorrelated velocities at rest with respect to the CMB. We use a new estimate of this mean peculiar velocity for the Hicken et al. (2009b) SN sample which is a slightly larger value of 0.5%. We account for this and assume an uncertainty of 0.1% resulting from a ± 0.2 error in the value of β.

The result is $H_0 = 74.8 \pm 3.0$ km s^{-1} Mpc^{-1}, a 4.0% measurement (top line, Table 4). It is instructive to deconstruct

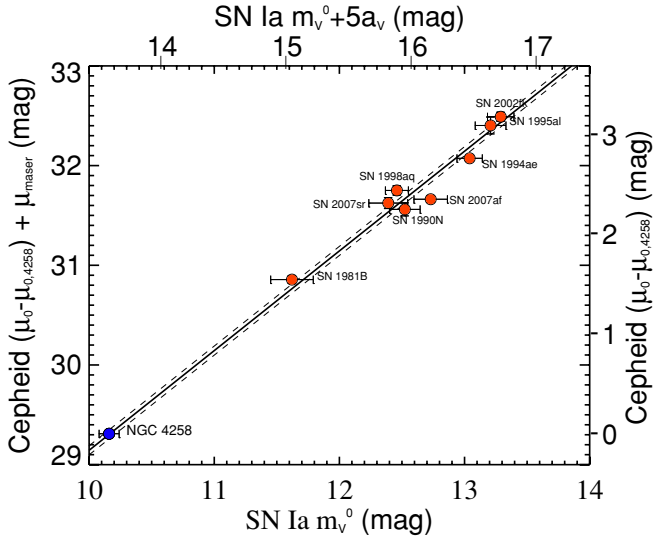

Figure 8. Relative distances from Cepheids and SNe Ia. The bottom abscissa shows the peak apparent visual magnitude of each SN Ia (red points) corrected for reddening and to the fiducial brightness (using the luminosity vs. light curve shape relations), m^0_V. The top abscissa includes the intercept of the m^0_V–log cz relation for SNe Ia, a_v, to provide SN Ia distance measures, $m^0_V + 5a_v$, quantities which are independent of the choice of a fiducial SN Ia. The right-hand ordinate shows the relative distances between the hosts determined from the Cepheid *VIH* Wesenheit relations. The left ordinate shows the same thing, with the addition of the independent geometric distance to NGC 4258 (blue point) based on its circumnuclear megamasers. The contribution of the nearby SN Ia and Cepheid data to H_0 can be expressed as a determination of $m^0_{V,4258}$, the theoretical mean of eight fiducial SNe Ia in NGC 4258. The dashed line indicates the uncertainty in the mean of the SN Ia hosts.

Table 4
Fits for H_0

$\chi^2_{\rm dof}$	No.	H_0	$<P$	a_v	M^0_V	[O/H]	$\delta M/\delta$[O/H]	b	$z_{\rm min}$	Fit	Scale	PLW	C R_V	SNe	SN R_V
0.65	448	**74.80(3.02)**	Y	0.697	−19.12	zkh	−0.25(0.10)	−3.02(0.06)	0.023	37	4258	$H_{V,I}$	3.1	*UBVRI*	2.5
0.65	448	75.62(3.05)	Y	0.702	−19.12	zkh	−0.25(0.10)	−3.02(0.06)	0.010	37	4258	$H_{V,I}$	3.1	*UBVRI*	2.5
0.64	497	76.03(3.02)	N	0.697	−19.09	zkh	−0.25(0.09)	−2.99(0.06)	0.023	37	4258	$H_{V,I}$	3.1	*UBVRI*	2.5
0.61	448	76.52(3.05)	Y	0.697	−19.07	zkh	−0.29(0.10)	−2.91(0.06)	0.023	37	4258	H	3.1	*UBVRI*	2.5
0.66	448	73.85(2.96)	Y	0.697	−19.15	zkh	···	−3.06(0.06)	0.023	37	4258	$H_{V,I}$	3.1	*UBVRI*	2.5
0.65	448	74.45(3.05)	Y	0.700	−19.15	zkh	−0.27(0.10)	−3.02(0.06)	0.023	61	4258	$H_{V,I}$	3.1	*BVRI*	2.5
1.87	570	76.16(3.83)	Y	0.697	−19.08	zkh	−0.27(0.15)	−2.89(0.09)	0.023	37	4258	$H_{V,I}$	3.1	*UBVRI*	2.5
0.65	448	74.52(3.04)	Y	0.701	−19.15	zkh	−0.24(0.10)	−3.02(0.06)	0.023	20	4258	$H_{V,I}$	3.1	*UBVRI*	3.1
0.64	448	75.12(3.02)	Y	0.697	−19.11	zkh	−0.26(0.10)	−3.00(0.06)	0.023	37	4258	$H_{V,I}$	2.5	*UBVRI*	2.5
0.65	448	74.83(3.00)	Y	0.690	−19.09	zkh	−0.26(0.10)	−3.02(0.06)	0.023	28	4258	$H_{V,I}$	3.1	*UBVRI*	2.0
0.66	448	75.00(2.99)	Y	0.684	−19.06	zkh	−0.27(0.10)	−3.02(0.06)	0.023	29	4258	$H_{V,I}$	3.1	*UBVRI*	1.5
0.64	448	73.42(3.04)	Y	0.691	−19.13	zkh	−0.22(0.10)	−3.03(0.06)	0.023	26	4258	$H_{V,I}$	3.1	*UBVRI*	2.5
0.64	448	74.71(3.11)	Y	0.699	−19.14	zkh	−0.25(0.10)	−3.02(0.06)	0.023	27	4258	$H_{V,I}$	3.1	*UBVRI*	3.1
0.65	497	75.92(2.99)	N	···	···	zkh	−0.25(0.09)	−3.00(0.06)	0.023	42	4258	$H_{V,I}$	3.1	*UBVRI*	···
0.64	497	76.25(2.99)	N	···	···	zkh	−0.25(0.09)	−2.97(0.06)	0.023	42	4258	$H_{V,I}$	2.5	*UBVRI*	···
0.65	448	74.80(3.02)	Y	0.697	−19.12	T_e	−0.37(0.15)	−3.02(0.06)	0.023	37	4258	$H_{V,I}$	3.1	*UBVRI*	2.5
0.76	514	**75.66(2.61)**	Y	0.697	−19.10	zkh	−0.20(0.11)	−3.19(0.03)	0.023	37	MW	$H_{V,I}$	3.1	*UBVRI*	2.5
0.76	514	76.49(2.63)	Y	0.702	−19.10	zkh	−0.20(0.11)	−3.19(0.03)	0.010	37	MW	$H_{V,I}$	3.1	*UBVRI*	2.5
0.75	563	76.70(2.58)	N	0.697	−19.07	zkh	−0.17(0.10)	−3.18(0.03)	0.023	37	MW	$H_{V,I}$	3.1	*UBVRI*	2.5
0.88	553	75.98(2.73)	Y	0.697	−19.09	zkh	−0.24(0.12)	−3.08(0.02)	0.023	37	MW	H	3.1	*UBVRI*	2.5
0.77	514	74.92(2.55)	Y	0.697	−19.12	zkh	···	−3.20(0.03)	0.023	37	MW	$H_{V,I}$	3.1	*UBVRI*	2.5
0.76	514	75.29(2.65)	Y	0.700	−19.13	zkh	−0.21(0.11)	−3.19(0.03)	0.023	61	MW	$H_{V,I}$	3.1	*BVRI*	2.5
1.86	636	77.58(4.07)	Y	0.697	−19.04	zkh	−0.19(0.15)	−3.14(0.04)	0.023	37	MW	$H_{V,I}$	3.1	*UBVRI*	2.5
0.76	514	75.38(2.64)	Y	0.701	−19.13	zkh	−0.19(0.11)	−3.19(0.03)	0.023	20	MW	$H_{V,I}$	3.1	*UBVRI*	3.1
0.75	514	76.10(2.60)	Y	0.697	−19.09	zkh	−0.20(0.11)	−3.17(0.03)	0.023	37	MW	$H_{V,I}$	2.5	*UBVRI*	2.5
0.77	514	75.70(2.58)	Y	0.690	−19.06	zkh	−0.20(0.11)	−3.19(0.03)	0.023	28	MW	$H_{V,I}$	3.1	*UBVRI*	2.0
0.77	514	75.88(2.56)	Y	0.684	−19.03	zkh	−0.21(0.11)	−3.19(0.03)	0.023	29	MW	$H_{V,I}$	3.1	*UBVRI*	1.5
0.76	514	74.29(2.66)	Y	0.691	−19.11	zkh	−0.16(0.11)	−3.19(0.03)	0.023	26	MW	$H_{V,I}$	3.1	*UBVRI*	2.5
0.76	514	75.56(2.72)	Y	0.699	−19.11	zkh	−0.20(0.11)	−3.19(0.03)	0.023	27	MW	$H_{V,I}$	3.1	*UBVRI*	3.1
0.76	563	76.62(2.53)	N	···	···	zkh	−0.17(0.10)	−3.18(0.03)	0.023	42	MW	$H_{V,I}$	3.1	*UBVRI*	···
0.75	563	77.05(2.52)	N	···	···	zkh	−0.18(0.10)	−3.16(0.03)	0.023	42	MW	$H_{V,I}$	2.5	*UBVRI*	···
0.76	514	77.72(3.15)	Y	0.697	−19.04	T_e	−0.29(0.16)	−3.19(0.03)	0.023	37	MW	$H_{V,I}$	3.1	*UBVRI*	2.5
0.75	514	**71.31(3.84)**	Y	0.697	−19.23	zkh	−0.20(0.11)	−3.19(0.03)	0.023	37	LMC	$H_{V,I}$	3.1	*UBVRI*	2.5
0.75	514	72.09(3.88)	Y	0.702	−19.23	zkh	−0.20(0.11)	−3.19(0.03)	0.010	37	LMC	$H_{V,I}$	3.1	*UBVRI*	2.5
0.73	563	72.46(3.82)	N	0.697	−19.19	zkh	−0.18(0.10)	−3.18(0.03)	0.023	37	LMC	$H_{V,I}$	3.1	*UBVRI*	2.5
0.86	553	69.68(3.91)	Y	0.697	−19.28	zkh	−0.24(0.11)	−3.08(0.02)	0.023	37	LMC	H	3.1	*UBVRI*	2.5
0.75	514	73.34(3.76)	Y	0.697	−19.17	zkh	···	−3.19(0.03)	0.023	37	LMC	$H_{V,I}$	3.1	*UBVRI*	2.5
0.75	514	70.76(3.85)	Y	0.700	−19.26	zkh	−0.21(0.11)	−3.19(0.03)	0.023	61	LMC	$H_{V,I}$	3.1	*BVRI*	2.5
1.84	636	72.70(5.31)	Y	0.697	−19.18	zkh	−0.19(0.15)	−3.14(0.04)	0.023	37	LMC	$H_{V,I}$	3.1	*UBVRI*	2.5
0.75	514	71.13(3.85)	Y	0.701	−19.25	zkh	−0.19(0.11)	−3.19(0.03)	0.023	20	LMC	$H_{V,I}$	3.1	*UBVRI*	3.1
0.74	514	71.37(3.83)	Y	0.697	−19.22	zkh	−0.21(0.11)	−3.17(0.03)	0.023	37	LMC	$H_{V,I}$	2.5	*UBVRI*	2.5
0.75	514	71.24(3.82)	Y	0.690	−19.20	zkh	−0.21(0.11)	−3.19(0.03)	0.023	28	LMC	$H_{V,I}$	3.1	*UBVRI*	2.0
0.76	514	71.26(3.82)	Y	0.684	−19.17	zkh	−0.22(0.11)	−3.19(0.03)	0.023	29	LMC	$H_{V,I}$	3.1	*UBVRI*	1.5
0.74	514	70.48(3.86)	Y	0.691	−19.22	zkh	−0.16(0.11)	−3.19(0.03)	0.023	26	LMC	$H_{V,I}$	3.1	*UBVRI*	2.5
0.74	514	71.23(3.90)	Y	0.699	−19.24	zkh	−0.20(0.11)	−3.19(0.03)	0.023	27	LMC	$H_{V,I}$	3.1	*UBVRI*	3.1
0.74	563	72.44(3.80)	N	···	···	zkh	−0.17(0.10)	−3.18(0.03)	0.023	42	LMC	$H_{V,I}$	3.1	*UBVRI*	···
0.73	563	72.51(3.79)	N	···	···	zkh	−0.18(0.10)	−3.16(0.03)	0.023	42	LMC	$H_{V,I}$	2.5	*UBVRI*	···
0.75	514	73.22(3.75)	Y	0.697	−19.17	T_e	−0.29(0.16)	−3.19(0.03)	0.023	37	LMC	$H_{V,I}$	3.1	*UBVRI*	2.5
0.76	514	**74.53(2.25)**	Y	0.697	−19.13	zkh	−0.19(0.11)	−3.20(0.03)	0.023	37	4258+MW	$H_{V,I}$	3.1	*UBVRI*	2.5
0.76	514	75.34(2.26)	Y	0.702	−19.13	zkh	−0.19(0.11)	−3.20(0.03)	0.010	37	4258+MW	$H_{V,I}$	3.1	*UBVRI*	2.5
0.75	563	75.61(2.23)	N	0.697	−19.10	zkh	−0.17(0.10)	−3.19(0.02)	0.023	37	4258+MW	$H_{V,I}$	3.1	*UBVRI*	2.5
0.88	553	75.48(2.39)	Y	0.697	−19.10	zkh	−0.24(0.12)	−3.08(0.02)	0.023	37	4258+MW	H	3.1	*UBVRI*	2.5
0.77	514	73.90(2.20)	Y	0.697	−19.15	zkh	···	−3.20(0.03)	0.023	37	4258+MW	$H_{V,I}$	3.1	*UBVRI*	2.5
0.76	514	74.15(2.30)	Y	0.700	−19.16	zkh	−0.21(0.11)	−3.20(0.03)	0.023	61	4258+MW	$H_{V,I}$	3.1	*BVRI*	2.5
1.86	636	75.90(3.44)	Y	0.697	−19.09	zkh	−0.18(0.15)	−3.15(0.04)	0.023	37	4258+MW	$H_{V,I}$	3.1	*UBVRI*	2.5
0.76	514	74.25(2.28)	Y	0.701	−19.16	zkh	−0.19(0.11)	−3.20(0.03)	0.023	20	4258+MW	$H_{V,I}$	3.1	*UBVRI*	3.1
0.75	514	74.92(2.24)	Y	0.697	−19.12	zkh	−0.20(0.11)	−3.18(0.03)	0.023	37	4258+MW	$H_{V,I}$	2.5	*UBVRI*	2.5
0.77	514	74.56(2.21)	Y	0.690	−19.10	zkh	−0.20(0.11)	−3.20(0.03)	0.023	28	4258+MW	$H_{V,I}$	3.1	*UBVRI*	2.0
0.77	514	74.72(2.19)	Y	0.684	−19.06	zkh	−0.21(0.11)	−3.20(0.03)	0.023	29	4258+MW	$H_{V,I}$	3.1	*UBVRI*	1.5
0.76	514	73.19(2.32)	Y	0.691	−19.14	zkh	−0.16(0.11)	−3.20(0.03)	0.023	26	4258+MW	$H_{V,I}$	3.1	*UBVRI*	2.5
0.76	514	74.43(2.38)	Y	0.699	−19.15	zkh	−0.19(0.11)	−3.20(0.03)	0.023	27	4258+MW	$H_{V,I}$	3.1	*UBVRI*	3.1
0.76	563	75.55(2.16)	N	···	···	zkh	−0.17(0.10)	−3.19(0.02)	0.023	42	4258+MW	$H_{V,I}$	3.1	*UBVRI*	···
0.75	563	75.93(2.15)	N	···	···	zkh	−0.17(0.10)	−3.17(0.02)	0.023	42	4258+MW	$H_{V,I}$	2.5	*UBVRI*	···
0.77	514	75.06(2.45)	Y	0.697	−19.12	T_e	−0.18(0.14)	−3.20(0.03)	0.023	37	4258+MW	$H_{V,I}$	3.1	*UBVRI*	2.5

Table 4
(Continued)

χ^2_{dof}	No.	H_0	$<P$	a_v	M^0_V	[O/H]	$\delta M/\delta$[O/H]	b	z_{min}	Fit	Scale	PLW	C R_V	SNe	SN R_V
0.75	514	**72.34(2.28)**	Y	0.697	−19.20	zkh	−0.17(0.10)	−3.19(0.03)	0.023	37	4258+LMC	$H_{V,I}$	3.1	*UBVRI*	2.5
0.75	514	73.13(2.30)	Y	0.702	−19.20	zkh	−0.17(0.10)	−3.19(0.03)	0.010	37	4258+LMC	$H_{V,I}$	3.1	*UBVRI*	2.5
0.73	563	73.45(2.26)	N	0.697	−19.16	zkh	−0.16(0.09)	−3.18(0.03)	0.023	37	4258+LMC	$H_{V,I}$	3.1	*UBVRI*	2.5
0.87	553	72.64(2.44)	Y	0.697	−19.19	zkh	−0.17(0.10)	−3.08(0.02)	0.023	37	4258+LMC	H	3.1	*UBVRI*	2.5
0.75	514	72.90(2.28)	Y	0.697	−19.18	zkh	···	−3.19(0.03)	0.023	37	4258+LMC	$H_{V,I}$	3.1	*UBVRI*	2.5
0.75	514	71.89(2.33)	Y	0.700	−19.23	zkh	−0.19(0.10)	−3.19(0.03)	0.023	61	4258+LMC	$H_{V,I}$	3.1	*BVRI*	2.5
1.84	636	73.41(3.50)	Y	0.697	−19.16	zkh	−0.18(0.14)	−3.14(0.04)	0.023	37	4258+LMC	$H_{V,I}$	3.1	*UBVRI*	2.5
0.75	514	72.10(2.31)	Y	0.701	−19.22	zkh	−0.17(0.10)	−3.19(0.03)	0.023	20	4258+LMC	$H_{V,I}$	3.1	*UBVRI*	3.1
0.74	514	72.56(2.28)	Y	0.697	−19.19	zkh	−0.18(0.10)	−3.17(0.03)	0.023	37	4258+LMC	$H_{V,I}$	2.5	*UBVRI*	2.5
0.75	514	72.32(2.25)	Y	0.690	−19.16	zkh	−0.18(0.10)	−3.19(0.03)	0.023	28	4258+LMC	$H_{V,I}$	3.1	*UBVRI*	2.0
0.76	514	72.42(2.24)	Y	0.684	−19.13	zkh	−0.19(0.10)	−3.19(0.03)	0.023	29	4258+LMC	$H_{V,I}$	3.1	*UBVRI*	1.5
0.74	514	71.24(2.36)	Y	0.691	−19.20	zkh	−0.14(0.10)	−3.19(0.03)	0.023	26	4258+LMC	$H_{V,I}$	3.1	*UBVRI*	2.5
0.74	514	72.25(2.40)	Y	0.699	−19.21	zkh	−0.17(0.10)	−3.19(0.03)	0.023	27	4258+LMC	$H_{V,I}$	3.1	*UBVRI*	3.1
0.74	563	73.42(2.22)	N	···	···	zkh	−0.15(0.09)	−3.18(0.03)	0.023	42	4258+LMC	$H_{V,I}$	3.1	*UBVRI*	···
0.73	563	73.64(2.21)	N	···	···	zkh	−0.16(0.09)	−3.16(0.03)	0.023	42	4258+LMC	$H_{V,I}$	2.5	*UBVRI*	···
0.75	514	73.13(2.29)	Y	0.697	−19.17	T_e	−0.29(0.16)	−3.19(0.03)	0.023	37	4258+LMC	$H_{V,I}$	3.1	*UBVRI*	2.5
0.77	514	**74.41(2.43)**	Y	0.697	−19.13	zkh	−0.09(0.09)	−3.20(0.03)	0.023	37	MW+LMC	$H_{V,I}$	3.1	*UBVRI*	2.5
0.77	514	75.23(2.45)	Y	0.702	−19.13	zkh	−0.09(0.09)	−3.20(0.03)	0.010	37	MW+LMC	$H_{V,I}$	3.1	*UBVRI*	2.5
0.75	563	75.43(2.40)	N	0.697	−19.10	zkh	−0.08(0.08)	−3.19(0.02)	0.023	37	MW+LMC	$H_{V,I}$	3.1	*UBVRI*	2.5
0.88	553	74.24(2.54)	Y	0.697	−19.14	zkh	−0.09(0.09)	−3.09(0.02)	0.023	37	MW+LMC	H	3.1	*UBVRI*	2.5
0.77	514	74.45(2.43)	Y	0.697	−19.13	zkh	···	−3.20(0.03)	0.023	37	MW+LMC	$H_{V,I}$	3.1	*UBVRI*	2.5
0.77	514	74.00(2.48)	Y	0.700	−19.16	zkh	−0.10(0.09)	−3.20(0.03)	0.023	61	MW+LMC	$H_{V,I}$	3.1	*BVRI*	2.5
1.86	636	76.14(3.78)	Y	0.697	−19.08	zkh	−0.09(0.13)	−3.15(0.04)	0.023	37	MW+LMC	$H_{V,I}$	3.1	*UBVRI*	2.5
0.76	514	74.15(2.46)	Y	0.701	−19.16	zkh	−0.09(0.09)	−3.20(0.03)	0.023	20	MW+LMC	$H_{V,I}$	3.1	*UBVRI*	3.1
0.76	514	74.74(2.43)	Y	0.697	−19.12	zkh	−0.09(0.09)	−3.18(0.03)	0.023	37	MW+LMC	$H_{V,I}$	2.5	*UBVRI*	2.5
0.77	514	74.42(2.40)	Y	0.690	−19.10	zkh	−0.10(0.09)	−3.20(0.03)	0.023	28	MW+LMC	$H_{V,I}$	3.1	*UBVRI*	2.0
0.78	514	74.56(2.38)	Y	0.684	−19.07	zkh	−0.11(0.09)	−3.20(0.03)	0.023	29	MW+LMC	$H_{V,I}$	3.1	*UBVRI*	1.5
0.76	514	73.21(2.50)	Y	0.691	−19.14	zkh	−0.07(0.09)	−3.20(0.03)	0.023	26	MW+LMC	$H_{V,I}$	3.1	*UBVRI*	2.5
0.76	514	74.30(2.55)	Y	0.699	−19.15	zkh	−0.09(0.09)	−3.20(0.03)	0.023	27	MW+LMC	$H_{V,I}$	3.1	*UBVRI*	3.1
0.76	563	75.41(2.35)	N	···	···	zkh	−0.08(0.08)	−3.19(0.02)	0.023	42	MW+LMC	$H_{V,I}$	3.1	*UBVRI*	···
0.75	563	75.73(2.34)	N	···	···	zkh	−0.08(0.08)	−3.17(0.02)	0.023	42	MW+LMC	$H_{V,I}$	2.5	*UBVRI*	···
0.77	514	75.37(2.64)	Y	0.697	−19.11	T_e	−0.13(0.13)	−3.20(0.03)	0.023	37	MW+LMC	$H_{V,I}$	3.1	*UBVRI*	2.5
0.77	514	**73.75(2.15)**	Y	0.697	−19.15	zkh	−0.10(0.09)	−3.21(0.03)	0.023	37	4258+MW+LMC	$H_{V,I}$	3.1	*UBVRI*	2.5
0.77	514	74.56(2.16)	Y	0.702	−19.15	zkh	−0.10(0.09)	−3.21(0.03)	0.010	37	4258+MW+LMC	$H_{V,I}$	3.1	*UBVRI*	2.5
0.75	563	74.82(2.12)	N	0.697	−19.12	zkh	−0.09(0.08)	−3.19(0.02)	0.023	37	4258+MW+LMC	$H_{V,I}$	3.1	*UBVRI*	2.5
0.88	553	74.26(2.28)	Y	0.697	−19.14	zkh	−0.09(0.09)	−3.09(0.02)	0.023	37	4258+MW+LMC	H	3.1	*UBVRI*	2.5
0.77	514	73.68(2.15)	Y	0.697	−19.16	zkh	···	−3.21(0.03)	0.023	37	4258+MW+LMC	$H_{V,I}$	3.1	*UBVRI*	2.5
0.77	514	73.34(2.21)	Y	0.700	−19.18	zkh	−0.11(0.09)	−3.21(0.03)	0.023	61	4258+MW+LMC	$H_{V,I}$	3.1	*BVRI*	2.5
1.86	636	75.08(3.29)	Y	0.697	−19.11	zkh	−0.10(0.13)	−3.16(0.04)	0.023	37	4258+MW+LMC	$H_{V,I}$	3.1	*UBVRI*	2.5
0.76	514	73.48(2.18)	Y	0.701	−19.18	zkh	−0.09(0.09)	−3.21(0.03)	0.023	20	4258+MW+LMC	$H_{V,I}$	3.1	*UBVRI*	3.1
0.76	514	74.07(2.14)	Y	0.697	−19.14	zkh	−0.10(0.09)	−3.18(0.02)	0.023	37	4258+MW+LMC	$H_{V,I}$	2.5	*UBVRI*	2.5
0.77	514	73.76(2.11)	Y	0.690	−19.12	zkh	−0.10(0.09)	−3.20(0.03)	0.023	28	4258+MW+LMC	$H_{V,I}$	3.1	*UBVRI*	2.0
0.78	514	73.90(2.09)	Y	0.684	−19.09	zkh	−0.11(0.09)	−3.20(0.03)	0.023	29	4258+MW+LMC	$H_{V,I}$	3.1	*UBVRI*	1.5
0.76	514	72.53(2.23)	Y	0.691	−19.16	zkh	−0.07(0.09)	−3.21(0.02)	0.023	26	4258+MW+LMC	$H_{V,I}$	3.1	*UBVRI*	2.5
0.76	514	73.64(2.28)	Y	0.699	−19.17	zkh	−0.10(0.09)	−3.21(0.02)	0.023	27	4258+MW+LMC	$H_{V,I}$	3.1	*UBVRI*	3.1
0.76	563	74.80(2.06)	N	···	···	zkh	−0.09(0.08)	−3.20(0.02)	0.023	42	4258+MW+LMC	$H_{V,I}$	3.1	*UBVRI*	···
0.75	563	75.12(2.06)	N	···	···	zkh	−0.09(0.08)	−3.17(0.02)	0.023	42	4258+MW+LMC	$H_{V,I}$	2.5	*UBVRI*	···
0.77	514	74.18(2.26)	Y	0.697	−19.14	T_e	−0.10(0.13)	−3.21(0.03)	0.023	37	4258+MW+LMC	$H_{V,I}$	3.1	*UBVRI*	2.5

the individual sources of uncertainty to improve our insight into the measurement. In principle, the covariance between the data and parameters does not allow for an exact and independent allocation of propagated error for each term toward the determination of H_0. However, in our case, the diagonal elements of the covariance matrices provide a very good approximation to the individual components of error. These are given in Table 5 and shown in Figure 9 for past and present determinations of H_0.

A number of improvements since R09 are evident by comparing Columns 2 and 3 in Table 5 and as shown in Figure 9. The uncertainty in H_0 from all of the terms independent of the megamaser distance to NGC 4258 is 2.3%, 50% smaller than these same terms in R09, a result of the increased sample of Cepheids and SN calibrators. This term includes uncertainties due to the form of the *P–L* relation, Cepheid metallicity dependences, photometry bias, and zero points—all of which were important systematic uncertainties in past determinations of the Hubble constant (see Column 1, which contains the values from Freedman et al. 2001). In this analysis, as in R09, these uncertainties have been reduced by the collection of samples of Cepheids whose measures (i.e., metallicity, periods, and photometric systems) are a good match between NGC 4258 and the SN hosts. Here the contribution from an unknown dependence of Cepheid luminosity on metallicity has been furthered reduced by 40% owing to a better match between the metallicity of the Cepheid samples in NGC 4258 and the expanded SN host sample. In R09, the mean metallicity

Table 5
H_0 Error Budget for Cepheid and SN Ia Distance Ladders[a]

Term	Description	Previous LMC	R09 N4258	Here N4258	Here All Three[b]
$\sigma_{\rm anchor}$	Anchor distance	5%	3%	3%	1.3%
$\sigma_{{\rm anchor}-PL}$	Mean of P–L in anchor	2.5%	1.5%	1.4%	0.7%[c]
$\sigma_{{\rm host}-PL}/\sqrt{n}$	Mean of P–L values in SN hosts	1.5%	1.5%	0.6 %	0.6%
$\sigma_{\rm SN}/\sqrt{n}$	Mean of SN Ia calibrators	2.5%	2.5%	1.9%	1.9%
σ_{m-z}	SN Ia m–z relation	1%	0.5%	0.5%	0.5%
$R\sigma_{\lambda,1,2}$	Cepheid reddening, zero points, anchor-to-hosts	4.5%	0.3%	0.0%	1.4%
σ_Z	Cepheid metallicity, anchor-to-hosts	3%	1.1%	0.6 %	1.0%
$\sigma_{\rm PL}$	P–L slope, $\Delta\log P$, anchor-to-hosts	4%	0.5%	0.4%	0.6%
$\sigma_{\rm WFPC2}$	WFPC2 CTE, long-short	3%	0%	0%	0%
Subtotal, σ_{H_0}		10%	4.7 %	4.0%	2.9%
Analysis systematics		NA	1.3%	1.0%	1.0%
Total, σ_{H_0}		10%	4.8 %	4.1%	3.1%

Notes.
[a] Derived from diagonal elements of the covariance matrix propagated via the error matrices associated with Equations (1), (3), (7), and (8).
[b] Using the combination of all three calibrations of the Cepheid distance scale, LMC, MW parallaxes, and NGC 4258.
[c] For MW parallax, this term is already included with the term above.

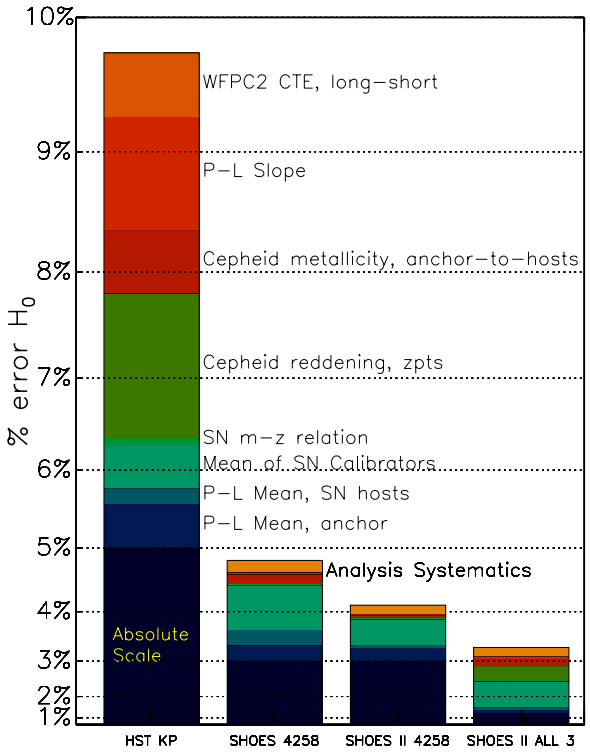

Figure 9. Uncertainties in the determination of the Hubble constant. Uncertainties are squared to show their contribution to the quadrature sum. These terms are given in Table 5.

of the NGC 4258 Cepheid sample on the ZKH abundance scale was $12 + \log[{\rm O/H}] = 8.91$, nearly the same as the present mean of 8.90. However, the mean metallicity of the Cepheid sample in the SN hosts has risen from 8.81 to 8.85. Some of this change can be attributed to the inclusion of Cepheids closer to the nuclei of the hosts and some to the inclusion of two new hosts, NGC 5584 and NGC 4038/9, with higher-than-average metallicities. The reduction in the mean abundance difference between NGC 4258 and the SN Ia hosts from 0.077 to 0.045 dex results in a decrease of the error propagated into H_0 from 1.1% to 0.6%. A similar reduction is seen with the use of MW Cepheids whose mean metallicity of 8.9 is closer to the mean of the new Cepheid sample in the SN hosts. We consider an alternative calibration of abundances from Bresolin (2011) in Section 4.1.

3.1. Buttressing the First Rung

In our present determination of H_0, the 3% uncertainty in the distance to NGC 4258 claimed by Greenhill (2009) is now greater than all other sources combined (in quadrature). The next largest term, the uncertainty in mean magnitude of the eight nearby SNe Ia, is 1.9%. To significantly improve upon our determination of H_0, we would need an *independent* calibration of the first rung of the distance ladder as good as or better than the megamaser-based measurement to NGC 4258 in terms of precision and reliability. Independent calibration of the first rung is also valuable as an alternative to NGC 4258, should future analyses reveal previously unidentified systematic errors affecting its distance measurement.

A powerful alternative has recently become available through high signal-to-noise ratio measurements of the trigonometric parallaxes of MW Cepheids using the fine guidance sensor (FGS) on *HST*. Benedict et al. (2007) reported parallax measurements for 10 Cepheids, with mean individual precision of 8% and an error in the mean of the sample of 2.5%. These were used in R09 as a test of the distance scale provided by NGC 4258, but the improvement in precision beyond the first rung in the previous section suggests greater value in their use to enhance the calibration of the first rung.

van Leeuwen et al. (2007) reanalyzed *Hipparcos* observations and determined independent parallax measurements for the same 10 Cepheids (albeit with half the precision of *HST*/FGS) and for three additional Cepheids (excluding Polaris which is an overtone pulsator and whose estimated fundamental period is an outlier among the Cepheids pulsing in the fundamental mode). The resulting sample can be considered an independent anchor with a mean, nominal uncertainty of just 1.7%. We use the combined parallaxes tabulated

by van Leeuwen et al. (2007) and their H-band photometry as an alternative to the Cepheid sample of NGC 4258 by replacing Equation (1) for the Cepheids in the hosts of SNe Ia with

$$m_{W,i,j} = \mu_{0,i} + M_{W,1} + b_W \log P_{i,j} + Z_W \Delta \log[\mathrm{O/H}]_{i,j}, \quad (6)$$

where $M_{W,1}$ is the absolute Wesenheit magnitude for a Cepheid with $P = 1$ day and simultaneously fitting the MW Cepheids with the relation

$$M_{W,i,j} = M_{W,1} + b_W \log P_{i,j} + Z_W \Delta \log[\mathrm{O/H}]_{i,j}. \quad (7)$$

Equation (3) for the SNe Ia is replaced with

$$m^0_{v,i} = \mu_{0,i} - M^0_V. \quad (8)$$

The determination of M^0_V for SNe Ia together with the previous term a_v then determines the Hubble constant,

$$\log H_0 = \frac{M^0_V + 5a_v + 25}{5}. \quad (9)$$

Since the near-IR magnitudes of these MW Cepheids have not been directly measured with WFC3, the use of these variables requires an additional allowance for possible differences in their photometry. These may arise from differences in instrumental zero points, crowding, filter transmission functions, and detector well depth at which the sources are measured together with an uncertainty in detector linearity. Analysis of the absolute photometry from WFC3–IR (Kalirai et al. 2009) and the ground system (e.g., Two Micron All Sky Survey; Skrutskie et al. 2006) claim absolute precision of 2%–3%. We therefore assume a *systematic* uncertainty in the relative magnitudes between *HST* WFC3 $F160W$ Cepheid photometry and the ground-based measurements of MW Cepheids on the H-band system of Persson et al. (1998) of 4%. This reduces the effective precision of the parallax distance scale from 1.7% to 2.6%. The ground-based photometry of these MW Cepheids is tabulated by Groenewegen (1999) and R09. This systematic error is included in the global fit as an additional calibration equation with uncertainty given in the error correlation matrix.

When using the MW Cepheids, we now include an external constraint on the slope of the near-IR P–L relation. No such constraint was necessary or even of significant value in the previous section because the Cepheid periods in NGC 4258 (mean $\log P = 1.51$) are so similar to those in the SN Ia host (mean $\log P = 1.63$). In contrast, the mean period of the MW sample (mean $\log P = 1.0$) is substantially lower, giving an unconstrained slope of the P–L relation a greater and unrealistically large lever arm. Following analyses of optical and near-IR Cepheid data in the MW (Fouqué et al. 2007) and the LMC (Persson et al. 2004; Udalski et al. 1999), we adopt a conservative constraint on the slope of the Wesenheit relation of -3.3 ± 0.1 mag dex^{-1} in $\log P$.

Using the MW Cepheids instead of NGC 4258 as the first rung of the distance ladder gives 75.7 ± 2.6 km s^{-1} Mpc^{-1}, in good agreement with (and even greater precision than) the NGC 4258-based value. However, an overall improvement in precision is realized by the *simultaneous* use of both the MW parallaxes and the megamaser-based distance to NGC 4258, yielding 74.5 ± 2.3 km s^{-1} Mpc^{-1}, a remarkably small uncertainty of 3.0%.

Another opportunity to improve upon the first rung on the distance ladder comes from the sample of H-band observations of Cepheids in the LMC by Persson et al. (2004). Recent studies of detached eclipsing binaries (DEBs) by different groups provide claims of a reliable and precise distance to the LMC. Guinan et al. (1998), Fitzpatrick et al. (2002), and Ribas et al. (2002) studied three B-type systems (HV2274, HV982, and EROS1044) which lie close to the bar of the LMC and therefore provide a good match to the Cepheid sample of Persson et al. (2004). The error-weighted mean of these is 49.2 ± 1.6 kpc.[12] Pietrzyński et al. (2009) analyzed OGLE-051019.64-685812.3, an eclipsing binary system comprised of two giant G-type stars also located near the barycenter of the LMC, and found a distance of 50.2 ± 1.3 kpc. The average result, 49.8 kpc, provides a good estimate of the distance to the LMC.[13] Here we retain the larger of the two previous uncertainties to estimate the distance modulus as 18.486 ± 0.065 mag or an effective error of ± 0.076 mag when including the aforementioned 0.04 mag uncertainty between the ground-based and *HST*-based near-IR photometric systems. Using this distance to the LMC and the Cepheid sample of Persson et al. (2004) yields 71.3 ± 3.8 km s^{-1} Mpc^{-1}, as seen in Table 4.

Combining all three first rungs (MW, LMC, and NGC 4258) provides the most precise measurement of H_0: 73.8 ± 2.1 km s^{-1} Mpc^{-1}, a slightly smaller uncertainty of 2.9%. As expected, the use of all three anchors for the distance ladder instead of just one has the largest impact on the overall uncertainty, reducing the total contribution of the first rung to the error from 3.3% to 1.5%. However, a substantial penalty is paid for the mixing of ground-based and space-based photometric systems and the resultant uncertainties in Wesenheit or dereddened magnitudes, adding a 1.4% error to H_0 where for NGC 4258 alone none pertained. Modest increases in error also result from the larger difference in mean Cepheid metallicity (LMC) and period (LMC and MW). See Figure 9 for the full error profile.

Past determinations of the absolute distance scale have had a checkered history, with revisions common. Thus, it may be prudent to rely on no more than any two of the three possible anchors of the distance scale in the determination of H_0. The omission of NGC 4258, MW parallaxes, or the LMC yields a precision in H_0 of 3.3%, 3.2%, and 3.0%, respectively. We thus adopt as our best determination 73.8 ± 2.3 km s^{-1} Mpc^{-1}, the measurement from all three sources of the distance scale, but with the larger error associated with only two independent origins of the distance scale.

Should future work revise the distance to any one of the absolute distance-scale determinations, we provide the following recalibration: H_0 decreases by 0.25, 0.30, and 0.14 km s^{-1} Mpc^{-1} for each increase of 1% in the distance to either NGC 4258, the MW parallax scale, or the distance to the LMC.

In the last column of Table 3, we also give the best estimate of the distance to each host from the global fit to all first rungs, Cepheid, and SN data. These are useful to compare to alternative methods of measuring distances to these hosts or to place a sample of relative measures of SNe Ia distances onto an absolute scale. For example, there has been recent disagreement on the

[12] A fourth system (Fitzpatrick et al. 2003; HV5936) is located several degrees away from the bar and yields a distance that is closer by 3σ. Additional lines of evidence presented in that paper suggest that this system lies above the disk of the LMC, i.e., closer to the Galaxy.

[13] However, we note the analysis by Schaefer (2008), who suggests a level of agreement in recent distance estimates to the LMC which is too good to be consistent with statistics.

distance modulus of the Antennae (NGC 4038/9); Saviane et al. (2008) claim a value of $\mu_0 = 30.62 \pm 0.17$ mag based on the apparent tip of the red giant branch (TRGB), while Schweizer et al. (2008) obtain $\mu_0 = 31.74 \pm 0.27$ mag from SN 2007sr and $\mu_0 = 31.51 \pm 0.16$ mag from a different determination of the TRGB, in agreement with previous estimates by Whitmore et al. (1999) and Tonry et al. (2000) based on flow-field models. Our result of $\mu_0 = 31.66 \pm 0.08$ mag (with the uncertainty based on the global fit) strongly favors the "long" distance to the Antennae.

Although we have been careful to propagate our statistical errors, as well as past sources of systematic error such as metallicity dependence, system zero point, and instrumental uncertainties, we now consider a broader range of systematic uncertainties relating to alternative approaches to the analysis of the data.

4. ANALYSIS SYSTEMATICS

In the preceding section, we presented our preferred approach to analyzing the Cepheid and SN Ia data, incorporating uncertainties within the framework used to model the data. Here we follow the same approach used by R09 to quantify the systematic uncertainty in the determination of H_0, by measuring the impact of a number of variants in the modeling of the Cepheid and SN Ia data.

In Table 4, we show 15 variants of the previously described analysis for every combination of choices of distance anchors (NGC 4258, MW, or LMC), any two of the preceding or all three; these amount to a total of 105 combinations. Our primary analysis for any anchor choice is given in the first row (shown in bold) for which that choice initially appears. Column 1 gives the value of χ^2_ν, Column 2 the number of Cepheids in the fit, Column 3 the value and total uncertainty in H_0, and Column 4 whether the near-IR data for Cepheids with periods shorter than the completeness limit from the optical selection were included. Column 5 gives the SN Ia magnitude–redshift intercept parameter, Column 6 gives the determination of M^0_V which is specific to the light curve fitter employed, Column 7 the calibration system for the metal abundances, Column 8 the value and uncertainty in the metallicity dependence, and Column 9 the value and uncertainty of the slope of the Cepheid *P–L* or *P–W* relation. Column 10 gives the minimum SN Ia redshift used to define the *m–z* relation, Column 11 encodes aspects of the SN fitting routine and assumptions therein addressed below, and Column 12 is the choice of anchors to set the distance scale. Column 13 gives the type of *P–L* relation employed, either Wesenheit (H, V, I) or the H band only. Column 14 is the reddening law value used for the Cepheids. Column 15 lists the filters allowed for fitting the SN Ia light curves and Column 16 gives the value of R_V used to fit the SN light curves.

4.1. Cepheid Systematics

In the preceding analysis of the Cepheid data, differences in the determination of H_0 may result from the following variants in the primary analysis: (1) retention of Cepheids with periods below the optical incompleteness limit, (2) not allowing for a metallicity dependence, (3) changing the Cepheid reddening law from $R_V = 3.1$ to $R_V = 2.5$, (4) using only near-IR magnitudes without reddening corrections, (5) no rejection of outliers in the *P–L* relations, and (6) a change in the calibration of chemical abundances. Each of these changes was implemented as a variant of the primary analysis with results given in Table 4. The rationale for the primary analysis over each variant was discussed in detail in Section 4 of R09, with the exception of (6) which is discussed below.

Taken individually, these variants result in H_0 rising or declining by $\lesssim$1.0 km s^{-1} Mpc^{-1}, which is less than half of the statistical uncertainty. A variant resulting in a larger change occurs when we do not reject Cepheids which are outliers on the *P–L* relation, raising H_0 by 1.3 km s^{-1} Mpc^{-1}. However, the value of χ^2_ν also triples, with a total increase in χ^2 of 6 per rejected outlier. As we expect outliers a priori to arise from blending or misidentification of Cepheids (type or period), resulting in residuals in excess of the typical uncertainty, we believe it is most sensible to reject them to minimize their impact on the global solution. The use of higher or lower thresholds for outlier rejection has even less impact than including all outliers. Lowering the outlier threshold to 2.25σ (and its accompanying residual magnitude) reduces H_0 by 0.1 km s^{-1} Mpc^{-1}. Raising the threshold to 3.0σ or 4.0σ reduces H_0 by 1.0 or 0.8 km s^{-1} Mpc^{-1}, respectively. Neglecting a reddening correction for the Cepheids also raises H_0 by 1.3 km s^{-1} Mpc^{-1} but we believe this correction is warranted.

As an alternative to rejecting outliers, we also considered the approach of simultaneously modeling the distribution of Cepheids and the outliers. Following Kunz et al. (2007), we allowed for a nuisance population of sources along the *P–L* relation characterized by a broader distribution ($\sigma = 1$ mag) and an intercept independent from that of classical Cepheids. The a posteriori likelihood function for the intercepts of the Cepheid hosts was then compared to that derived from outlier rejection. The mean zero point of the SN hosts is greater by 0.013 ± 0.012 mag. The mean uncertainty of the intercepts is a factor of 1.38 greater than those from outlier rejection but still small compared to the distance precision of each SN. The only difference of note (i.e., >0.03 mag) was for the intercept of NGC 4536 which was greater by 0.08 ± 0.05 mag in the outlier modeling over the use of rejection.

The chemical abundance values for the Cepheids used in R09 and here were estimated from nebular lines in H II regions of the Cepheid hosts using the R_{23} parameter and the transformation to an oxygen abundance following Zaritsky et al. (1994, hereafter ZKH). There are several alternative calibrations of the transformation from R_{23} to log [O/H] (e.g., McGaugh 1991; Pilyugin & Thuan 2005), but these primarily affect the absolute normalization of the metallicity scale and do not alter the relative host-to-host differences in abundance or the determination of H_0. Recently, Bresolin (2011) has redetermined the abundance gradient of NGC 4258 by adopting the Pilyugin & Thuan (2005) calibration of R_{23}. This calibration yields abundances that are consistent with those determined directly by Bresolin (2011) in four H II regions in the outer disk of NGC 4258, measuring the electron temperature (T_e) via the auroral line [O III] λ 4363. Given this agreement, Bresolin (2011) suggests the adoption of a so-called T_e scale for the determination of absolute chemical abundances of extragalactic Cepheids.

The T_e recalibration of nebular oxygen abundances not only reduces the values of log [O/H] by $\sim$ 0.4 dex at the metal-rich end but also compresses the abundance scale by a factor of 0.69. Based on this scale and consistent atomic data, Bresolin (2011) finds a nebular oxygen abundance for the LMC of $12 + \log [O/H] = 8.36$, moderately lower than the "canonical" value of 8.5 in the ZKH scale. On the T_e scale, the mean apparent metallicity of the SN Ia and maser hosts would be $12 + \log [O/H] = 8.42$; this is closer to the LMC Cepheids

than to the MW Cepheids and a departure from the ZKH scale. While the abundances of MW Cepheids are not measured the same way (i.e., they are based on stellar absorption lines rather than on nearby ionized gas), they have been directly measured to be ∼0.3 dex higher than those of LMC Cepheids (Andrievsky et al. 2002; Romaniello et al. 2008). The resulting estimate of 8.66 for the MW Cepheids on the T_e scale would agree well with recent estimates of the solar oxygen abundance of 8.69 (Asplund et al. 2009) together with a small gradient in metallicity away from the solar neighborhood. This LMC to MW Cepheid abundance difference of 0.3 dex also agrees well with the T_e scale compression of the 0.4 dex difference on the ZKH scale for which the value for MW Cepheids was taken (here and in R09) to be 8.9.

We determined the effect on H_0 of a change from the ZKH scale to the T_e scale by transforming the values of 12+log [O/H] using Equation (3) of Bresolin (2011) and assigning values of 8.36 and 8.66 to LMC and MW Cepheids, respectively. As seen in Table 4, the value of H_0 increases by 0.4 km s^{-1} Mpc^{-1} when using all three calibrators and increases by less than 1.0 km s^{-1} Mpc^{-1} for any combination of two calibrators. The biggest change, an increase of 2.0 km s^{-1} Mpc^{-1}, occurs when only the MW is used to calibrate the first rung, a direct consequence of the increase of the metallicity difference between the SN Ia host and MW Cepheids on the T_e scale. In the presence of uncertainties concerning the appropriate values of Cepheid abundances, the determination of H_0 based on *infrared* observations of Cepheids should be significantly less sensitive to metallicity differences than optical Cepheid data (Marconi et al. 2005). Indeed, the metallicity correction empirically determined here, -0.10 ± 0.09 mag dex^{-1} (using all three calibrations), is less than half the value of ~ -0.25 mag dex^{-1} measured at optical wavelengths (Kennicutt et al. 1998; Sakai et al. 2004) and its absolute value is not significant. A better determination of the difference in metallicity between MW and extragalactic Cepheids may not occur until the launch of the *James Webb Space Telescope* (*JWST*).

4.2. SN Systematics

Here we consider the following variants in the analysis of the SN Ia data: (1) minimum range of SN Ia m–z relation lowered from $z = 0.023$ to $z = 0.01$, (2) discarding U-band SN Ia light curve data (fit 61), (3) SN Ia reddening parameter $R_V = 1.5, 2.0, 3.1$ (fits 29, 28, and 20), (4) use of an SN Ia luminosity–color correction with no prior (i.e., as in the β parameter of SALT II instead of an extinction parameter, R_V, in MLCS2k2) (fit 26), (5) a host-galaxy extinction likelihood prior from galaxy simulations (fit 27), and (6) use of the SALT-II light curve fitter (fit 42). The motivation for these variants is described in greater detail in R09.

As seen in Table 4, none of these variants taken individually alters the value of H_0 by more than ∼1.5 km s^{-1} Mpc^{-1} from the preferred solution, less than half the statistical uncertainty. One of the more noteworthy variants is the use of the SALT-II light curve fitter (Guy et al. 2005) in lieu of MLCS2k2, since the result of this change can be substantial for high-redshift data (Kessler et al. 2009). Observations of high-redshift SNe Ia typically have lower signal-to-noise ratios and thus place greater reliance on fitters and on the assumptions they include (e.g., the relation between SN Ia color and distance). In contrast, the determination of H_0 is quite *insensitive* to the fitter; the use of SALT-II results in an increase in H_0 of 1 km s^{-1} Mpc^{-1}.

The dispersion of the 15 different determinations of H_0 is 0.7 or 0.8 km s^{-1} Mpc^{-1} for any selected pair of sources of the absolute distance scale. Adding this measure of analysis systematics to the previous yields 73.8 ± 2.4 km s^{-1} Mpc^{-1}, a 3.3% uncertainty, our best determination.

5. DARK ENERGY AND NEUTRINOS

An independent and precise measurement of H_0 is an important complement to the determination of cosmological model parameters. Alternatively, it serves as a powerful test of model-constrained measurements at higher redshifts. It is beyond the scope of this paper to provide a complete analysis of the impact of the measurement of H_0 on the cosmological model from all extant data. We encourage others to do so. However, one such example using the present measurement of H_0 can be illustrative.

Making use of the simplest present hypothesis for the cosmological model (namely Λ-cold-dark-matter without curvature, exotic neutrino physics, or specific early-universe physics), and using the single most powerful cosmological data set (the 7 year *WMAP* results from Komatsu et al. 2011), results in a predicted value of $H_0 = 71.0 \pm 2.5$ km s^{-1} Mpc^{-1}. This value agrees well with our determination of 73.8 ± 2.4 km s^{-1} Mpc^{-1} at better than the combined 1σ confidence level.

Alternatively, we can use the *WMAP* data together with the measured value of H_0 to constrain added complexity to the model. In Figure 10, we show the use of this data combination for constraining a redshift-independent dark energy equation-of-state parameter (w), the number of relativistic species (e.g., neutrino number), and the sum of neutrino masses. The result for dark energy is $w = -1.08 \pm 0.10$, about 20% more precise than the same result derived from the determination of H_0 in R09. If we had perfect knowledge of the CMB, our overall 30% increase in the precision of H_0 would yield the same-sized improvement in the determination of w. However, the fractional uncertainty in $\Omega_M h^2$ from the *WMAP* 7 year analysis is comparable to our measurement of H_0; thus, greater precision in w may still be wrung from future higher-precision measurements of the CMB by *WMAP* or *Planck*.

The enhanced precision in measuring H_0 also provides a strong rebuff to recent attempts to explain accelerated expansion without dark energy but rather by our presence in the center of a massive void of gigaparsec scale. Already such models are hard to fathom as they require an exotic location for the observer, at the center of the void to within a part in a million (Blomqvist & Mörtsell 2010) to avoid an excess dipole in the CMB. It is also not yet apparent if such a model is consistent with other observables of the CMB or the late-time-integrated Sachs–Wolfe effect. However, using measurements of $H(z > 1)$ to constrain void models of the Lemaitre, Tolmon, and Bondi variety already predicts slower-than-observed local expansion with values of $H_0 = 60$ (Nadathur & Sarkar 2010) or 62 (Wiltshire 2007) km s^{-1} Mpc^{-1}, more than 5σ below our measurement.

Comparable improvements to cosmological constraints on relativistic species are also realized from R09, as shown in Figure 10. Most interesting may be the effective number of relativistic species, $N_{\rm eff} = 4.2 \pm 0.75$, which is nominally higher than the value of 3.046 expected from the three known neutrino species plus tau-neutrino heating from e^+e^- collisions (Mangano & Serpico 2005). While this nominal excess of relativistic species has been noted previously (e.g., Reid et al. 2010; Komatsu et al. 2011; Dunkley et al. 2010), and even interpreted as a possible indication of the presence of a sterile neutrino (Hamann et al. 2010), we caution that the cosmological

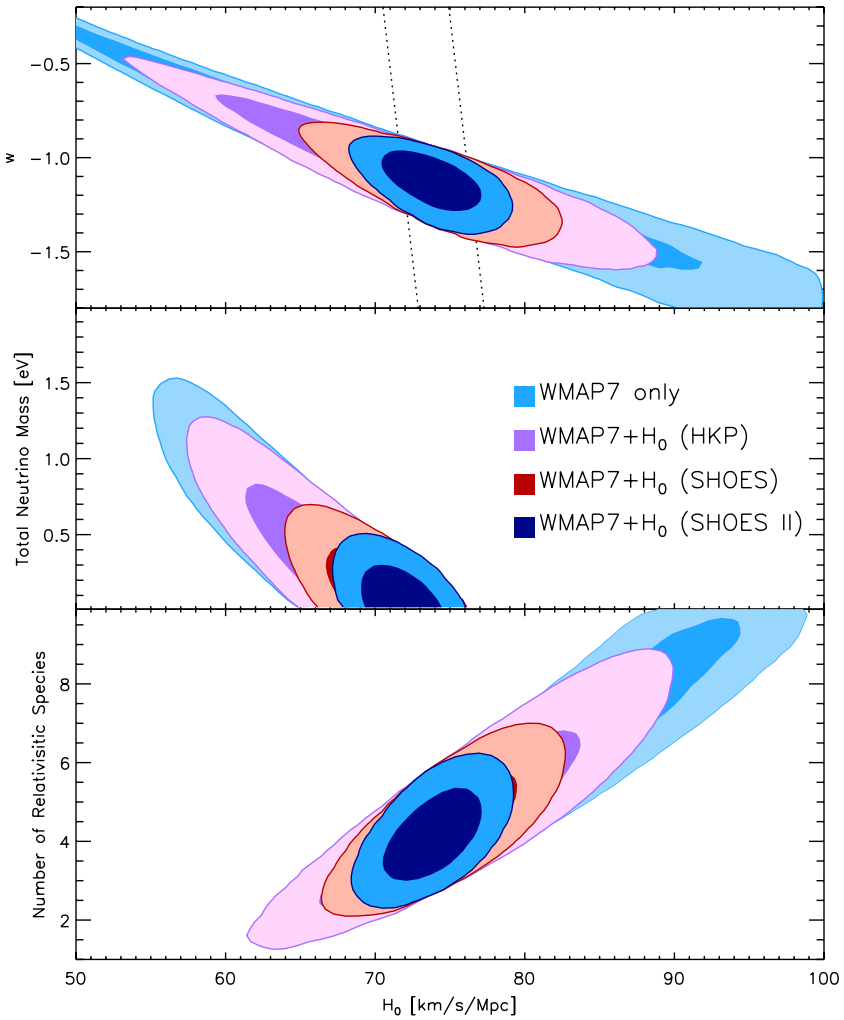

Figure 10. Confidence regions in the plane of H_0 and the equation-of-state parameter of dark energy, w, and neutrino properties. The localization of the third acoustic peak in the *WMAP* 7 year data (Komatsu et al. 2011) produces a confidence region which is narrow but highly degenerate with the dark energy equation of state (upper panel). The improved measurement of H_0, 73.8 ± 2.6 km s^{-1} Mpc^{-1}, from the SH0ES program is complementary to the *WMAP* constraint, resulting in a determination of $w = -1.08 \pm 0.10$ assuming a constant w. This result is comparable in precision to determinations of w from baryon acoustic oscillations and high-redshift SNe Ia, but is independent of both. The inner regions are 68% confidence and the outer regions are 95% confidence. The modest tilt of the SH0ES measurement of 0.2% in H_0 for a change in w of 0.1 shown as the dotted lines in the upper panel results from the mild dependence of a_v on w, corresponding to the change in H for changes from $w = -1$ at the mean SN redshift of $z = 0.04$. The measurement of H_0 is made at $j_0 = 1$ (i.e., $w = -1$). Constraints on the mass and number of relativistic species (e.g., neutrinos) are shown in the middle and lower panels, respectively.

model provides other avenues for reducing the significance of this result including additional degrees of freedom for curvature, dark energy, primordial helium abundance, and neutrino masses. The 30% improvement in the present constraint on H_0 combined with improved high-resolution CMB data (e.g., Dunkley et al. 2010) and ultimately with *Planck* satellite CMB data should reduce the present uncertainty in $N_{\rm eff}$ by a factor of ~ 3 which may provide a more definitive conclusion on the presence of excess radiation in the early universe.

6. DISCUSSION

Examination of the complete error budget for H_0 in the last two columns of Table 5 indicates additional approaches for improved precision in future measurements of H_0. Expanding the sample of well-measured parallaxes to MW Cepheids (especially those at $\log P > 1$) with the *GAIA* satellite could drive the precision of the first rung of the distance ladder well under 1%. However, as we have found with the "baker's dozen" of present MW parallaxes, much of this precision would be lost without better cross-calibration between the space and ground photometric systems used to measure Cepheids, near and far.

The largest remaining term comes from the quite limited sample of ideal SN Ia calibrators, just eight objects. The occurrence of an ideal SN Ia in the small volume within which *HST* can measure Cepheids ($R \approx 30$ Mpc) is rare, on average only once every 2–3 years. Given the recent proliferation of SN surveys and instances of multiple, independent discoveries, we are confident that all such SNe Ia within this volume are being found. Collecting more will require extending the range of Cepheid measurements—without introducing new systematics—and patience. The forthcoming *JWST* offers a promising route to extend Cepheid observations out to 50 Mpc and to redder wavelengths, where uncertainties due to possible variations in the extinction law and the dependence of Cepheid luminosities on metallicity are further reduced. This extension would increase the SN sample suitable for calibration by a factor of ~5, reaching ~40 ideal SNe Ia observed over the past 20 years. Based on a 5% distance precision per ideal SN, such a sample would enable a determination of H_0 to better than

1%. However, discovering these Cepheids may require imaging at optical wavelengths where the amplitude of the variations is significant, a requirement which will challenge the short-wavelength capabilities of the *JWST*.

7. SUMMARY AND CONCLUSIONS

We have improved upon the precision of the measurement of H_0 from Riess et al. (2009a) by (1) more than doubling the sample of Cepheids observed in the near-IR in SN Ia host galaxies, (2) expanding the SN Ia sample from six to eight with the addition of SN 2007af and SN 2007sr, (3) increasing the sample of Cepheids observed in NGC 4258 by 20%, (4) reducing the difference in metallicity for the observed sample of Cepheids between the calibrator and the SN hosts, and (5) calibrating all optical Cepheid colors with WFC3 to remove cross-instrument zero-point errors. Further improvements to the precision and reliability of the measurement of H_0 come from the use of additional sources of calibration for the first rung; foremost of these are the trigonometric parallaxes of 13 Cepheids in the MW.

Our primary analysis gives $H_0 = 73.8 \pm 2.4$ km s^{-1} Mpc^{-1} including systematic errors determined from varying assumptions and priors used in the analysis. The combination of this result alone with the *WMAP* 7 year constraints yields $w = -1.08 \pm 0.10$ and improves constraints on a possible but still uncertain excess in relativistic species above the number of known neutrino flavors. The measured H_0 is also highly inconsistent with the simplest inhomogeneous matter models invoked to explain the apparent acceleration of the universe without dark energy. Given that statistical errors still dominate over systematic errors, future work is likely to further improve the precision of the determination of H_0.

We are grateful to William Januszewski for his help in executing this program on *HST*. We are indebted to Mike Hudson for assisting with the peculiar-velocity calculations from the PSCz survey, to David Larson for contributions to the *WMAP* MCMC analysis, to Daniel Scolnic for donating some useful routines, and to Mark Huber for an analysis of pre-discovery observations of SN 2007sr. Financial support for this work was provided by NASA through programs GO-11570 and GO-10802 from the Space Telescope Science Institute, which is operated by AURA, Inc., under NASA contract NAS 5-26555. A.V.F.'s supernova group at U. C. Berkeley is also supported by NSF grant AST-0607485 and by the TABASGO Foundation. L.M. acknowledges support from a Texas A&M University faculty startup fund. The metallicity measurements for NGC 5584 and NGC 4038/9 presented herein were obtained with the W. M. Keck Observatory, which is operated as a scientific partnership among the California Institute of Technology, the University of California, and NASA; the observatory was made possible by the generous financial support of the W. M. Keck Foundation. We thank Chris Kochanek and Kris Stanek for their support of GO-11570.

REFERENCES

Andrievsky, S. M., et al. 2002, A&A, 381, 32
Argon, A. L., Greenhill, L. J., Reid, M. J., Moran, J. M., & Humphreys, E. M. L. 2007, ApJ, 659, 1040
Asplund, M., Grevesse, N., Sauval, A. J., & Scott, P. 2009, ARA&A, 47, 481
Benedict, G. F., et al. 2007, AJ, 133, 1810
Blomqvist, M., & Mörtsell, E. 2010, J. Cosmol. Astropart. Phys., JCAP05(2010)006
Branchini, E., et al. 1999, MNRAS, 308, 1
Bresolin, F. 2011, ApJ, 729, 56
Cardelli, J. A., Clayton, G. C., & Mathis, J. S. 1989, ApJ, 345, 245
Dunkley, J., et al. 2010, arXiv e-prints
Fitzpatrick, E. L., Ribas, I., Guinan, E. F., DeWarf, L. E., Maloney, F. P., & Massa, D. 2002, ApJ, 564, 260
Fitzpatrick, E. L., Ribas, I., Guinan, E. F., Maloney, F. P., & Claret, A. 2003, ApJ, 587, 685
Fouqué, P., et al. 2007, A&A, 476, 73
Freedman, W. L., & Madore, B. F. 2010, ARA&A, 48, 673
Freedman, W. L., et al. 2001, ApJ, 553, 47
Ganeshalingam, M., et al. 2010, ApJS, 190, 418
Gibson, B. K. 2000, Mem. Soc. Astron. Ital., 71, 693
Gibson, B. K., et al. 2000, ApJ, 529, 723
Greenhill, L. 2009, Astro2010: The Astronomy and Astrophysics Decadal Survey, Science White Papers, 103
Groenewegen, M. A. T. 1999, A&AS, 139, 245
Guinan, E. F., et al. 1998, ApJ, 509, L21
Guy, J., Astier, P., Nobili, S., Regnault, N., & Pain, R. 2005, A&A, 443, 781
Hamann, J., Hannestad, S., Raffelt, G. G., Tamborra, I., & Wong, Y. Y. Y. 2010, Phys. Rev. Lett., 105, 181301
Herrnstein, J. R., et al. 1999, Nature, 400, 539
Hicken, M., Wood-Vasey, W. M., Blondin, S., Challis, P., Jha, S., Kelly, P. L., Rest, A., & Kirshner, R. P. 2009a, ApJ, 700, 1097
Hicken, M., et al. 2009b, ApJ, 700, 331
Hui, L., & Greene, P. B. 2006, Phys. Rev. D, 73, 123526
Humphreys, E. M. L., Argon, A. L., Greenhill, L. J., Moran, J. M., & Reid, M. J. 2005, in ASP Conf. Ser. 340, Future Directions in High Resolution Astronomy, ed. J. Romney & M. Reid (San Francisco, CA: ASP), 466
Humphreys, E. M. L., Reid, M. J., Greenhill, L. J., Moran, J. M., & Argon, A. L. 2008, ApJ, 672, 800
Jha, S., Riess, A. G., & Kirshner, R. P. 2007, ApJ, 659, 122
Kalirai, J. S., et al. 2009, The Photometric Calibration of WFC3: SMOV and Cycle 17 Observing Plan, Tech. Rep., Space Telescope Science Institute
Kelly, P. L., Hicken, M., Burke, D. L., Mandel, K. S., & Kirshner, R. P. 2010, ApJ, 715, 743
Kennicutt, R. C., Jr., et al. 1998, ApJ, 498, 181
Kessler, R., et al. 2009, ApJS, 185, 32
Komatsu, E., et al. 2011, ApJS, 192, 18
Kunz, M., Bassett, B. A., & Hlozek, R. A. 2007, Phys. Rev. D, 75, 103508
Lampeitl, H., et al. 2010, ApJ, 722, 566
Macri, L. M., Stanek, K. Z., Bersier, D., Greenhill, L. J., & Reid, M. J. 2006, ApJ, 652, 1133
Madore, B. F. 1982, ApJ, 253, 575
Madore, B. F., & Freedman, W. L. 1991, PASP, 103, 933
Mangano, G., & Serpico, P. D. 2005, Nucl. Phys., 145, 351
Marconi, M., Musella, I., & Fiorentino, G. 2005, ApJ, 632, 590
McGaugh, S. S. 1991, ApJ, 380, 140
Nadathur, S., & Sarkar, S. 2010, arXiv e-prints
Neill, J. D., Hudson, M. J., & Conley, A. 2007, ApJ, 661, L123
Neill, J. D., et al. 2009, ApJ, 707, 1449
Perlmutter, S., et al. 1999, ApJ, 517, 565
Persson, S. E., Madore, B. F., Krzemiński, W., Freedman, W. L., Roth, M., & Murphy, D. C. 2004, AJ, 128, 2239
Persson, S. E., Murphy, D. C., Krzeminski, W., Roth, M., & Rieke, M. J. 1998, AJ, 116, 2475
Pietrzyński, G., et al. 2009, ApJ, 697, 862
Pike, R. W., & Hudson, M. J. 2005, ApJ, 635, 11
Pilyugin, L. S., & Thuan, T. X. 2005, ApJ, 631, 231
Reid, B. A., Verde, L., Jimenez, R., & Mena, O. 2010, J. Cosmol. Astropart. Phys., JCAP01(2010)003
Ribas, I., Fitzpatrick, E. L., Maloney, F. P., Guinan, E. F., & Udalski, A. 2002, ApJ, 574, 771
Riess, A. G., Davis, M., Baker, J., & Kirshner, R. P. 1997, ApJ, 488, L1
Riess, A. G., et al. 1998, AJ, 116, 1009
Riess, A. G., et al. 2005, ApJ, 627, 579
Riess, A. G., et al. 2007, ApJ, 659, 98
Riess, A. G., et al. 2009a, ApJ, 699, 539
Riess, A. G., et al. 2009b, ApJS, 183, 109
Romaniello, M., et al. 2008, A&A, 488, 731
Saha, A., Sandage, A., Labhardt, L., Tammann, G. A., Macchetto, F. D., & Panagia, N. 1996, ApJ, 466, 55
Saha, A., Sandage, A., Labhardt, L., Tammann, G. A., Macchetto, F. D., & Panagia, N. 1997, ApJ, 486, 1

Saha, A., Sandage, A., Tammann, G. A., Dolphin, A. E., Christensen, J., Panagia, N., & Macchetto, F. D. 2001, ApJ, 562, 314
Sakai, S., Ferrarese, L., Kennicutt, R. C., Jr., & Saha, A. 2004, ApJ, 608, 42
Sandage, A., Tammann, G. A., Saha, A., Reindl, B., Macchetto, F. D., & Panagia, N. 2006, ApJ, 653, 843
Saviane, I., Momany, Y., da Costa, G. S., Rich, R. M., & Hibbard, J. E. 2008, ApJ, 678, 179
Schaefer, B. E. 2008, AJ, 135, 112
Schweizer, F., et al. 2008, AJ, 136, 1482
Skrutskie, M. F., et al. 2006, AJ, 131, 1163
Soszyński, I., Gieren, W., & Pietrzyński, G. 2005, PASP, 117, 823
Stetson, P. B., & Gibson, B. K. 2001, MNRAS, 328, L1
Sullivan, M., et al. 2010, MNRAS, 406, 782
Tonry, J. L., Blakeslee, J. P., Ajhar, E. A., & Dressler, A. 2000, ApJ, 530, 625
Udalski, A., Soszynski, I., Szymanski, M., Kubiak, M., Pietrzynski, G., Wozniak, P., & Zebrun, K. 1999, Acta Astron., 49, 223
van Leeuwen, F., Feast, M. W., Whitelock, P. A., & Laney, C. D. 2007, MNRAS, 379, 723
Whitmore, B. C., Zhang, Q., Leitherer, C., Fall, S. M., Schweizer, F., & Miller, B. W. 1999, AJ, 118, 1551
Wiltshire, D. L. 2007, Phys. Rev. Lett., 99, 251101
Zaritsky, D., Kennicutt, R. C., Jr., & Huchra, J. P. 1994, ApJ, 420, 87